Denudation Process of Crystalline Nappes in a Continental Collision Zone Constrained by Inversion of Fission - Track Data and Thermokinematic Forward Modeling: An Example From Eastern Nepalese Himalaya

AUTHOR(S):

Nakajima, Toru; Kawakami, Tetsuo; Iwano, Hideki; Danhara, Tohru; Sakai, Harutaka

JGR Solid Earth

RESEARCH ARTICLE
10.1029/2021JB023630

Denudation Process of Crystalline Nappes in a Continental Collision Zone Constrained by Inversion of Fission-Track Data and Thermokinematic Forward Modeling: An Example From Eastern Nepalese Himalaya

Toru Nakajima[1,2], Tetsuo Kawakami[1], Hideki Iwano[3], Tohru Danhara[3], and Harutaka Sakai[1]

[1]Department of Geology and Mineralogy, Graduate School of Science, Kyoto University, Kyoto, Japan, [2]Tono Geoscience Center, Japan Atomic Energy Agency, Gifu, Japan, [3]Kyoto Fission-Track Co., Ltd, Kyoto, Japan

Key Points:

- Inversion of fission-track data and forward thermokinematic modeling were applied to reconstruct the denudation history of eastern Nepal
- Observed gradual-rapid-gradual cooling time-temperature paths were reproduced by the model assuming the flat-ramp-flat structure of the MHT
- Our result indicates that the denudation pattern has roughly been constant in southeastern Nepal since ca. 9 Ma

Supporting Information:

Supporting Information may be found in the online version of this article.

Correspondence to:

T. Nakajima,
nakajima.toru@jaea.go.jp

Citation:

Nakajima, T., Kawakami, T., Iwano, H., Danhara, T., & Sakai, H. (2022). Denudation process of crystalline nappes in a continental collision zone constrained by inversion of fission-track data and thermokinematic forward modeling: An example from eastern Nepalese Himalaya. *Journal of Geophysical Research: Solid Earth*, *127*, e2021JB023630. https://doi.org/10.1029/2021JB023630

Received 21 NOV 2021
Accepted 23 APR 2022

Author Contributions:

Conceptualization: Toru Nakajima, Tetsuo Kawakami, Harutaka Sakai
Data curation: Hideki Iwano, Tohru Danhara
Formal analysis: Toru Nakajima
Funding acquisition: Tetsuo Kawakami, Harutaka Sakai
Investigation: Toru Nakajima, Harutaka Sakai

Abstract Thermochronological methods were applied to the Higher Himalayan Crystalline (HHC) nappe and the underlying Lesser Himalayan Sequences (LHS) to elucidate the denudation process for the middle- and upper-crust of eastern Nepal over millions of years. Thermochronological inverse modeling was undertaken for new results of fission-track (FT) age and FT length data of zircon and apatite in order to reconstruct the time-temperature (*t-T*) paths in the temperature range of 60–350°C. Eight *t-T* paths calculated along the across-strike section show that the cooling process of the HHC nappe in this study area is characterized by the following three aspects: (a) gradual cooling followed by rapid cooling and subsequent gradual cooling, (b) northward-younging of the timing of the rapid cooling, and (c) gradual cooling followed by <2 Myr rapid cooling in the frontmost part of the HHC nappe. The observed FT ages and *t-T* paths were then compared with those predicted by forwarding thermokinematic modeling. The results of the thermokinematic modeling for the "Flat-Ramp-Flat MHT model", in which the HHC and the underlying LHS are denudated in direct proportion to the uplift of rocks transported along the Main Himalayan Thrust (MHT), reproduced the observed *t-T* paths and FT ages in eastern Nepal. This indicates that the observed FT ages and *t-T* paths reflect a denudation process driven by the movement of the MHT with a flat-ramp-flat geometry and that the denudation rate and its spatial distribution have roughly been constant in eastern Nepal since ca. 9 Ma.

Plain Language Summary Motion of the deep-seated rocks toward earth's surface (exhumation/denudation) in continental collision zones is a key phenomenon to understanding the mechanism of mountain building associated with a continental collision. Thermochronological method enables us to reconstruct the cooling history of the rock samples and address their denudation history of them. In this study, we collected metamorphic rocks from eastern Nepal and succeeded in reconstructing a detailed cooling history. The observed cooling history was compared with the predicted cooling history derived from numerical modeling of three different denudation processes. As a result, the observed cooling history in eastern Nepal was explained well by denudation associated with the movement of a stable, single plate-boundary fault. This indicates that the denudation style of the deep-seated rocks in eastern Nepal was established about 9 million years ago and remained unchanged since then. This finding contributes to understanding mountain building process that affects shallow crustal levels.

1. Introduction

The Himalayas are the modern example of orogen associated with a continent-continent collision and have been the subject of many studies as a natural laboratory to understand continental collision processes. Thermochronology has been a quite common way to constrain the denudation history of the convergent orogen (Reiners & Ehlers, 2005). It has been applied to the Himalayas since the 1990s to understand denudation processes, and as a result, a large number of thermochronological data have been published (Thiede & Ehlers, 2013 and references therein). The abundant thermochronological datasets coupled with numerical experiments demonstrate that orogen-wide denudation over millions of years is controlled primarily by tectonics, and erosion plays a subordinate role. Several tectono-thermal models have been proposed to explain the denudation process of the mountain range (Bollinger et al., 2006; Coutand et al., 2014; Herman et al., 2010; Landry et al., 2016; Robert et al., 2011; van der Beek et al., 2016; Whipp et al., 2007; Wobus et al., 2006).

Methodology: Toru Nakajima, Hideki Iwano, Tohru Danhara
Project Administration: Tetsuo Kawakami, Harutaka Sakai
Resources: Tohru Danhara
Supervision: Tetsuo Kawakami, Harutaka Sakai
Visualization: Toru Nakajima
Writing – original draft: Toru Nakajima
Writing – review & editing: Tetsuo Kawakami, Hideki Iwano, Tohru Danhara

Previously published thermochronological studies on the Himalayas have focused on the distribution of the cooling ages along an elevation profile (Arita & Ganzawa, 1997; Blythe et al., 2007; Huntington et al., 2006; Streule et al., 2012) or along an across-strike section (Grujic et al., 2006; Nakajima et al., 2020b; Robert et al., 2009) in order to understand the interaction between tectonics and the cooling process. Thermochronometers record the time after the rocks cooled below the effective closure temperature (Dodson, 1973), and the distribution pattern of thermochronological ages represents a motion of the tectonic unit within a thermal field of the crust. However, in principle, specific cooling history cannot be uniquely reconstructed from cooling ages alone, because the closure temperature varies as a function of grain size and cooling rate within the partial anneal (or retention) zone (PAZ: e.g., Gleadow et al., 1986). Therefore, in spite of a numerous published thermochronological age datasets, different tectono-thermal models have been proposed to explain the same data. As such, there has been little consensus on a single tectonic process that primarily drove denudation. The distribution pattern of the thermochronological ages has been interpreted to reflect the following four tectono-thermal processes: (a) tectonically-driven denudation associated with the movement of the plate boundary fault (e.g., Robert et al., 2009), (b) enhanced denudation associated with the underplating of the Indian crust and growth of the duplex (e.g., Bollinger et al., 2004), (c) focused denudation in the high-mountain range accompanied by the Quaternary slip on the splay fault of the plate boundary fault (e.g., Arita & Ganzawa, 1997), and (d) large-scale thermal perturbation followed by thermal relaxation associated with the rapid over thrusting of the high-grade metamorphic rocks (e.g., Sakai, Iwano, Danhara, Hirata, et al., 2013; see Section 2.3 for detailed review of this process). In some regions, the same thermochronological datasets are explained by different tectono-thermal models (e.g., central Nepal: Ghoshal et al., 2020; Herman et al., 2010; Robert et al., 2009). This situation shows the limitation of the studies based solely on the thermochronological ages and their distribution patterns, and evaluation of the tectonic models by another approach with the high-temporal resolution is required.

The thermochronological inverse analysis (e.g., Ketcham, 2005) is a powerful approach that enables us to reconstruct the cooling process with high-temporal resolution. In this study, we applied the thermochronological inverse analysis method to the samples from the Himalayas to improve the temporal resolution of the thermal history reproduced. The zircon and apatite fission-track (ZFT/AFT) age determination and fission-track (FT) length measurement were newly carried out, and the thermochronological inverse analysis of these data was performed to reconstruct the time-temperature (*t-T*) path of each rock sample in the temperature range of 60–350°C (e.g., Ketcham, 2019). This is the first work to perform the ZFT-AFT multi-system inversion for the reconstruction of the *t-T* path in the Himalayas. This type of analysis was carried out for eight locations along the across-strike section from the Higher Himalayan Crystalline (HHC) nappe distributed in eastern Nepal to elucidate its detailed thermal history. We also performed the forward modeling of the FT ages and *t-T* paths using a thermokinematic model (Braun, 2003; Braun et al., 2012) in order to discuss the interaction between the tectonics and cooling processes. The combined approach of the FT analyses and the thermokinematic modeling helped quantify the primary factor that drove the denudation in eastern Nepal since Middle Miocene. In this study, we use the term "exhumation" to represent the vertical particle motion relative to Earth's surface and "denudation" including a horizontal component of the particle motion (reviewed by Ring et al. [1999]).

2. Geological Background

2.1. Overview of the Geology of the Central and Eastern Himalayas

The Himalayas are generally divided into four geotectonic units: the Tethys Himalayan Sequences (THS), the Higher Himalayan Crystallines (HHC: so-called the Greater Himalayan Sequences), the Lesser Himalayan Sequences (LHS), and the sub-Himalaya. These geotectonic units are separated by four north-dipping large-scale shear zones: from the north to the south, are the South Tibetan Detachment (STD), the Main Central Thrust (MCT), the Main Boundary Thrust (MBT), and the Main Frontal Thrust (MFT; Figure 1a).

The THS are mainly composed of unmetamorphosed carbonate and siliciclastic sedimentary rocks ranging in depositional age from Paleozoic to Paleogene (Bordet et al., 1971). The THS are separated from the HHC by the normal-sense STD shear zone. The HHC are composed of the high-grade metamorphic rocks and the Miocene leucogranites. The kyanite- and sillimanite-grade metamorphic rocks of the HHC underwent Cenozoic metamorphism (Inger & Harris, 1992; Pecher, 1989) and were intruded by Miocene leucogranite. The HHC and the LHS are separated by the ductile shear zone, MCT. The HHC overthrust onto the LHS to form the HHC nappe, which structurally covers a ~100 km-wide and ~2,000 km-long area of the LHS in the Lesser Himalayan mountain

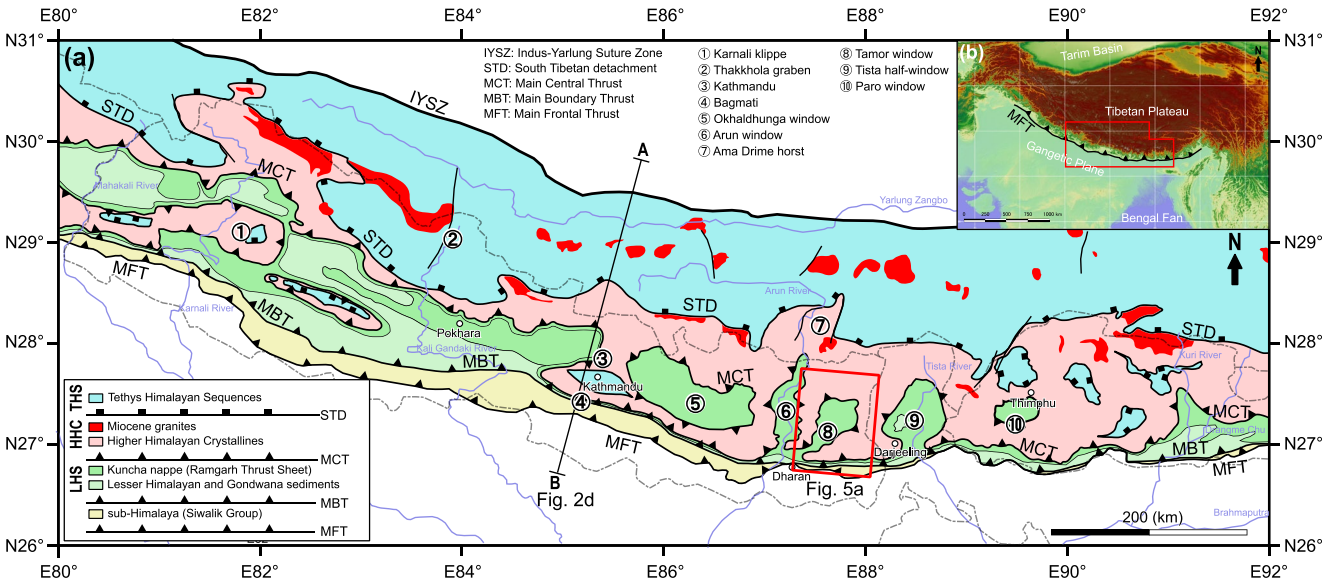

Figure 1. (a) Geotectonic map of the Central and Eastern Himalayas after DeCelles et al. (2020), Long et al. (2011), and Soucy La Roche (2018). A-B represents the position of the geotectonic transect shown in Figure 2d. A red rectangle indicates the study area and map area of Figure 5a. Circled numbers represent the locations of other study areas mentioned in the text. THS, Tethys Himalayan Sequence; HHC, Higher Himalayan Crystallines; LHS, Lesser Himalayan Sequences. (b) Digital elevation model (DEM) image (ALOS World 3D-30 m provided by the Japan Aerospace Exploration Agency) of southern Asia with the location of Figure 1a.

range (the Lesser Himalaya). The regional-scale nappes and klippes are mainly distributed at axial parts of the EW-trending synforms, with tectonic windows commonly developed at the center of the antiforms (Figures 1a and 2d). The LHS is composed of unmetamorphosed sedimentary rocks and low-to medium-grade metamorphic rocks that thrust onto the sub-Himalaya along the MBT. Further subdivisions of the HHC and the LHS in eastern Nepal are described in detail in Section 2.4. The sub-Himalaya consists of a foreland basin fill of the Siwalik sediments that were deposited during the middle Miocene to early Pleistocene (e.g., Appel et al., 1991). The MCT, the MBT, and the MFT are interpreted to root into a single crustal decollement, the Main Himalayan Thrust (MHT: Figure 2d; e.g., Schelling & Arita, 1991).

2.2. Geological and Geophysical Constraints on the Geometry and Activity of the Main Himalayan Thrust

The short-term bedrock uplift and denudation processes (10^0–10^3 yr) in the Himalayas have been discussed mainly based on a large number of geophysical observations on current shortening and deformations accommodated in the plate boundary fault. Geodetic and seismic studies have shown that the Indian sub-continent is presently underthrusting beneath the southern Tibet (e.g., Zhao et al., 1993) with the fault marking the plate boundary between the Indian sub-continent and the Eurasian continent termed the MHT (Figure 2d). Receiver Function studies have also suggested that the MHT is traceable as a continuous structure into the upper- and middle crust across the Central and Eastern Himalayas (Mitra et al., 2005; Nábělek et al., 2009; Schulte-Pelkum et al., 2005).

Geodetic studies demonstrate ongoing crustal shortening and bedrock uplift resulting from the active faulting of the MHT (Ader et al., 2012; Berger et al., 2004; Bilham et al., 1997; Grandin et al., 2012; Jackson & Bilham, 1994; Jouanne et al., 2004; Figure 2a), and have further constrained its geometry in the upper- and middle-crust. These studies argue that the geometry of the current MHT is characterized by a flat-ramp-flat geometry with the two major ramps (Figure 2d). One is a very shallow, frontmost ramp that corresponds to the MFT, and another is a mid-crustal ramp located beneath the frontal part of the high-mountain range of the Himalayas. The flat-ramp-flat geometry of the MHT is also indicated by the millennial-scale exhumation rate distribution estimated by the geomorphic studies (Lavé & Avouac, 2000, 2001). The estimated locations, number, and slopes of the mid-crustal ramps vary along the Himalayas (Berger et al., 2004; Hubbard et al., 2016; Robert et al., 2011; X. Wang et al., 2017) with some geophysical studies even suggesting that the mid-crustal ramp does not exist in the Nepalese Himalaya (Avouac et al., 2015; Schulte-Pelkum et al., 2005).

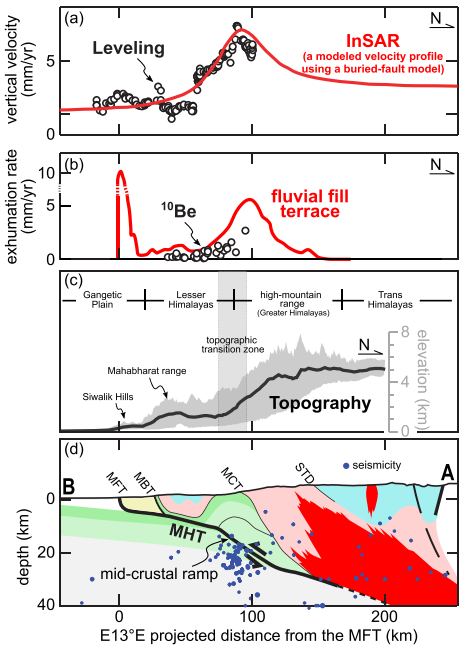

Figure 2. (a) Vertical velocity distributions along across-strike sections derived from InSAR (Grandin et al., 2012) and leveling (Jackson & Bilham, 1994) in western-central and central Nepal, respectively. The red heavy line was calculated using a buried-fault model to fit the InSAR data by Grandin et al. (2012). (b) Millennial-scale exhumation rate distribution derived from a geomorphic modeling (Lave & Avouac, 2001) and ^{10}Be dating (Godard et al., 2014; Olen et al., 2015). (c) Average topographic profile (thick solid line) with minimum and maximum elevations (shaded area) in central Nepal. The topographic transition zone marks a sharp topographic break between the Lesser Himalaya and the high-mountain range (Higher Himalaya). (d) Geotectonic transect of central Nepal along A-B in Figure 1a modified after Lavé & Avouac (2001). STD, South Tibetan Detachment; MCT, Main Central Thrust; MBT, Main Boundary Thrust; MFT, Main Frontal Thrust; MHT, Main Himalayan Thrust.

In addition to geophysical studies, geological studies have also contributed to understanding the geometry of the MHT. Geological mapping combined with the balancing cross-section method illustrated a crustal-scale duplex structure of the LHS and decollement below the duplex in far-western Nepal (Lesser Himalayan Duplex: e.g., DeCelles et al., 2001). Although such duplex structures cannot be necessarily detected throughout the Himalaya, the Lesser Himalayan Duplex is believed to lie beneath the antiform recognized across the Nepalese Himalaya (DeCelles et al., 2020; Khanal & Robinson, 2013; Pearson & DeCelles, 2005), the Sikkim Himalaya (Bhattacharyya & Mitra, 2009), and the Bhutanese Himalaya (Long et al., 2011; McQuarrie et al., 2014). These studies suggest that the MHT exhibits a similar flat-ramp-flat geometry as the geodetic studies indicate, however, the mid-crustal ramp is often depicted in the southern edge of the duplex rather than beneath the frontal part of the Himalayan high-mountain range.

The 2015 M_w 7.8 Gorkha earthquake provided an opportunity to explore the detailed structure of the MHT, and a number of geodetic and seismic studies reexamined the geometry of the MHT in central Nepal (Duputel et al., 2016; Elliott et al., 2016; Whipple et al., 2016). The activity of the splay faults rooting into the MHT (Whipple et al., 2016) and the existence of the duplex structure at the middle-crustal depths (Mendoza et al., 2019) were proposed and have been actively debated since then. Additionally, new balanced cross-sections were generated to reconcile geology with the new geophysical datasets (Ghoshal et al., 2020; Hubbard et al., 2016).

Geodetic and geomorphic studies have revealed the current convergence rate between the Indian and the Eurasian plates to be approximately 20 mm/yr (Ader et al., 2012; Bettinelli et al., 2006; Bilham et al., 1997; Lavé & Avouac, 2000; Mukul et al., 2010). On the other hand, a change in the convergence rate over a geologic time-scale (10^6–10^7 yr) is suggested by the balanced cross-section (McQuarrie et al., 2014) and thermochronological studies (Coutand et al., 2014).

2.3. Tecto-Thermal Models Proposed by Thermochronological Studies

In order to understand the denudation process on a geologic time-scale (10^6–10^7 yr), a number of thermochronological studies from the Central and Eastern Himalayas have generated a large number of ZFT and AFT ages (Figure 3). Most of the ZFT and AFT ages range from ca. 16 to ca. 1 Ma, indicating the Neogene and Quaternary rapid exhumation of the Himalayas. The accumulated FT ages along across-strike sections exhibit symmetrical concave-up patterns in age versus across-strike distance diagram, with the youngest FT age located at the topographic transition zone south of the high-mountain range (Figure 3). Thermochronological studies have focused on these characteristic age patterns to elucidate the cooling history of the geological bodies (e.g., Robert et al., 2011). Four major tecto-thermal models have been proposed to explain the concave-up FT age distribution patterns. These models are briefly introduced in the following sections.

2.3.1. The Overthrusting Model

The most widely accepted tectono-thermal model termed the Overthrusting model here, suggests that the movement of the MHT tectonically controls the denudation of the Himalaya, and areal variation of the exhumation rate mainly reflects the geometry of the MHT (Coutand et al., 2014; Robert et al., 2009, 2011). In this model, the concave-up pattern of the FT ages results from the difference in the exhumation rate between a high-rate area above the mid-crustal ramp of the MHT and a low-rate area above the flat of the MHT (Figure 4a). This tectonic model is designed based on the geophysical observations and has a good agreement with the areal variation of bedrock uplift rates and inferred kinematics of the MHT. These models were proposed mainly to explain

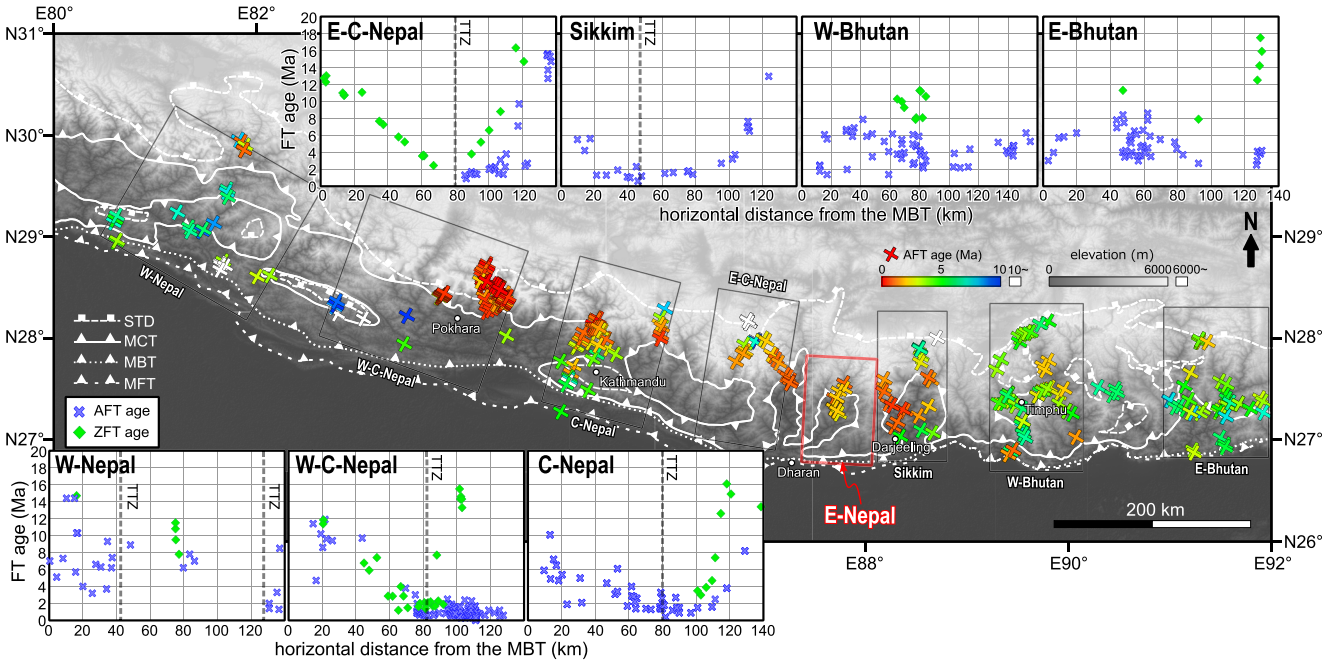

Figure 3. The Digital Elevation Model image of the Central and Eastern Himalayas, with the published apatite fission track and zircon fission track ages (western Nepal - DeCelles et al., 2020; Sakai, Iwano, Danhara, Hirata, et al., 2013; van der Beek et al., 2016: western-central Nepal - Blythe et al., 2007; Crouzet et al., 2007; DeCelles et al., 2020; Huntington et al., 2006; Nadin & Martin, 2012; Nakajima et al., 2020a: central Nepal - Herman et al., 2010; Robert et al., 2009; A. Wang et al., 2010: eastern-central Nepal - Carrapa et al., 2016; Nakajima et al., 2020b; Sakai et al., 2005; Streule et al., 2012: eastern Nepal - Larson et al., 2017; Sakai, Iwano, Danhara, Takigami, et al., 2013: Sikkim - Landry et al., 2016: western Bhutan - Coutand et al., 2014; Grujic et al., 2006; McQuarrie et al., 2014: eastern Bhutan - Coutand et al., 2014; Grujic et al., 2006; Long et al., 2012). Symbol markers are color-coded to reflect the apatite fission track (AFT) age of each point. Major geotectonic boundaries are drawn in white lines. Seven diagrams illustrate the zircon fission track and AFT age distributions along across-strike sections of the boxed areas. TTZ = topographic transition zone.

the thermochronology of central Nepal and eastern and western Bhutan, and have been shown to be consistent with both the thermochronology and geophysical data from each region. In addition, inverse analysis using the thermokinematic model provides quantitative constraints on the geometry and slip rate of the MHT (Coutand et al., 2014; Robert et al., 2011). On the other hand, this model does not take local fault activities and fold growths into account, which can be common in the Himalayas. Moreover, this model assumes the geometry of current MHT to have been stable for a geologic time-scale of 10^6–10^7 yr without any supporting evidence.

2.3.2. The Lesser Himalayan Duplex Model

This tectono-thermal model takes the development of the Lesser Himalayan Duplex into account (Ghoshal et al., 2020; Gilmore et al., 2018; Landry et al., 2016; McQuarrie & Ehlers, 2015; McQuarrie et al., 2019). The geometry of the MHT is not stable, and a thrust sheet accretes from the footwall to the hanging wall of the MHT, which is accompanied by the forward sequential propagation of the MHT (Figure 4b). In this model, enhanced denudation accompanied by the duplex growth results in a symmetrical FT age pattern above the duplex. This model was designed based on the balanced cross-section method (e.g., Dahlstrom, 1969), and thus related to the tectonic history of the LHS. Previous studies mentioned above reproduced the cooling age distribution pattern using thermokinematic model coupled with a balanced cross-section and discussed the timing of duplex growth and its impact on the upper-crustal denudation (e.g., McQuarrie & Ehlers, 2015). The timing of the growth of the Lesser Himalayan Duplex varies according to studies and regions. In the Nepalese Himalaya, geological studies suggest that the growth of the Lesser Himalayan Duplex was initiated in middle Miocene and terminated in Pliocene (DeCelles et al., 2001, 2020; Khanal et al., 2015) or Pleistocene (Ghoshal et al., 2020; Hubbard et al., 2016). McQuarrie and Ehlers (2015) and McQuarrie et al. (2019), on the other hand, suggest that the growth of the duplex had already terminated in Miocene in the Bhutanese Himalaya.

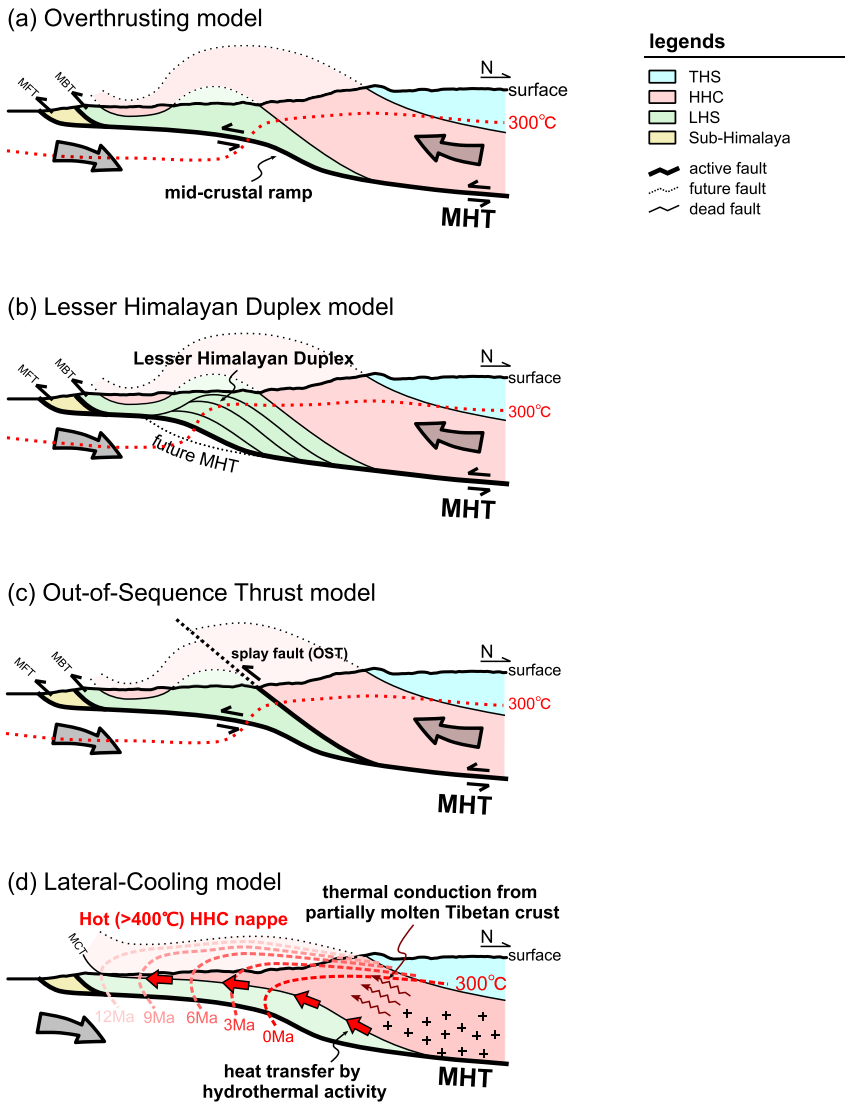

Figure 4. Schematic diagrams of four major tectono-thermal models interpreting the concave-up FT age distribution; (a) Overthrusting model, (b) Lesser Himalayan Duplex model, (c) Out-of-Sequence Thrust model, and (d) Lateral-Cooling model.

2.3.3. The Out-of-Sequence Thrust Model

The Out-of-Sequence Thrust model takes into account the enhanced uplift accompanied by the movement of splay thrusts rooting into the MHT (Figure 4c). The out-of-sequence thrust activity has been indicated based on the high uplift and exhumation rates in the high-mountain range located ~100 km north of the deformation front of the MFT (Arita & Ganzawa, 1997; Blythe et al., 2007; Hodges et al., 2004; Whipple et al., 2016; Wobus et al., 2003). Huntington et al. (2006) argued that the offset of the cooling ages was caused by the out-of-sequence faulting of the thrust which has been confirmed by field-based mapping in central Nepal. This finding reveals that splay fault activity strongly contributes to enhanced denudation in some areas. On the other hand, recent thermochronological studies demonstrate that no significant FT age gap exists between the hanging wall and the footwall of the out-of-sequence thrust in west-central and central Nepal (Nadin & Martin, 2012; Nakajima et al., 2020a; Robert et al., 2011), and that contribution of the out-of-sequence thrust activity to the fast denudation in the high-mountain range is not always supported.

2.3.4. The Lateral-Cooling Model

A completely different tectono-thermal model from the above three, termed the Lateral-Cooling model, explains that the northward-younging of the FT ages resulted from the gradual cooling of the "hot" HHC nappe from the frontal part to the root part that took place after the southward extrusion and emplacement of the HHC nappe (Figure 4d: Sakai, 2005; Sakai, Iwano, Danhara, Hirata, 2013; Sakai, Iwano, Danhara, Takagami, et al., 2013; Soucy La Roche, 2018). In this model, the HHC rapidly extruded as a ductile body at a temperature higher than 400°C (Nakajima et al., 2020a) and progressively cooled from the frontal part to the root part, both during and after the extrusion and emplacement. Sakai, Iwano, Danhara, Hirata, et al. (2013) proposed that the LHS exposed at the surface was overthrust by the "hot" HHC nappe and underwent thermal metamorphism. Sakai (2015) and Nakajima et al. (2020a) explained that the slow, post-emplacement lateral-cooling of the HHC nappe and the LHS was enabled by the heat supply from the root part in partially melted the middle crust of Tibet to the frontal part via thermal conduction and fluid flow along the MCT. This hypothesis is yet to be tested numerically. In addition, these studies did not mention how the erosion has progressed since the HHC nappe covered the LHS.

2.4. Geology of Eastern Nepal

2.4.1. The Higher Himalayan Crystallines and the Main Central Thrust

The HHC distributed in eastern Nepal is divided into the Upper HHC and the Lower HHC (Figure 5a), bounded by the reverse-sense ductile shear zone of the High Himal Thrust (HHT: Goscombe et al., 2006). The Upper HHC mainly consists of sillimanite gneiss, cordierite gneiss, and granitic orthogneiss intruded by the plutons, dykes, and sills of the Miocene leucogranite (Goscombe & Hand, 2000). The Upper HHC experienced high-temperature (T) and low-pressure (P) metamorphism at ca. 33–25 Ma under the P-T conditions of <6–8 kbar and 750–800°C (Ambrose et al., 2015; Imayama et al., 2012, 2019). The leucogranite emplacement and intrusion of dykes mainly occurred at ca. 24–17 Ma in eastern-central and eastern Nepal (Catlos et al., 2002; Harrison et al., 1999). The Lower HHC, bounded by the MCT at its base and by the HHT at its top, mainly consists of kyanite gneiss, sillimanite gneiss, metaquartzite, and amphibolite of the Junbesi Paragneiss (Schelling, 1992) that equates to Formation I (Le Fort, 1975) in central Nepal. The Lower HHC is considered to have undergone the high-T and moderate-P metamorphism (8–14 kbar, 720–770°C) at ca. 25–18 Ma (Ambrose et al., 2015; Imayama et al., 2012). The HHC nappe, which structurally covers an extensive area of eastern Nepal, is equivalent to the Lower HHC and also underwent moderate P-T metamorphism (ca. 11 kbar, ~670°C: Groppo et al., 2009; Kawakami et al., 2019). All rock samples from the HHC collected in this study are pelitic and psammitic gneisses, equivalent to Formation I.

The thrust fault movement along the HHT and exhumation of the Upper HHC are considered to have occurred at ca. 27–19 Ma (Imayama et al., 2012). After the termination of the HHT activity, the Upper and Lower HHC overthrusts onto the LHS until ca. 12 Ma, which was accompanied by the slip of the MCT (Ambrose et al., 2015; Larson et al., 2017). These age constraints are consistent with the Th-Pb monazite age of ca. 11 Ma obtained from the MCT zone in eastern-central Nepal and the Sikkim Himalayas (Catlos et al., 2001, 2004), although ca. 8 Ma Th-Pb monazite age obtained from the MCT zone of the LHS in eastern-central Nepal Himalaya is interpreted to represent the ca. 8 Ma reactivation of the MCT (Kohn et al., 2001).

The structural position of the MCT has been described differently in previous studies; at the base of the migmatitic gneiss (Schelling, 1992) or at the base of the Sisne Khola augen gneiss (Goscombe et al., 2006). In this study, we locate the MCT at the base of the migmatitic gneiss following the stratigraphic and geotectonic divisions by Schelling (1992) based on the detailed investigation of the distribution of the lithology and ductile deformation in the Dhankuta area (Figure 5a) by Sato et al. (2019).

2.4.2. The Lesser Himalayan Sequences, the Main Boundary Thrust, and the Main Frontal Thrust

The LHS distributed in eastern Nepal are divided into three geotectonic units; the Lesser Himalayan (LH) para-autochthon, the Kuncha nappe, and the MCT zone. The LH para-autochthon is composed of the Paleoproterozoic sediments of the Lower Nawakot Group (~2,500 m thick: Kobayashi et al., 2021; Rai et al., 2016) and the Gondwana and post-Gondwana foreland basin sediments of the Tansen Group (~2,400 m thick: Sakai, 1983). The Kuncha nappe is separated from the LHS para-autochthon by the Lesser Himalayan Thrust (known as the Ramgarh Thrust: Pearson & DeCelles, 2005) at its base. The Kuncha nappe is composed of the Proterozoic

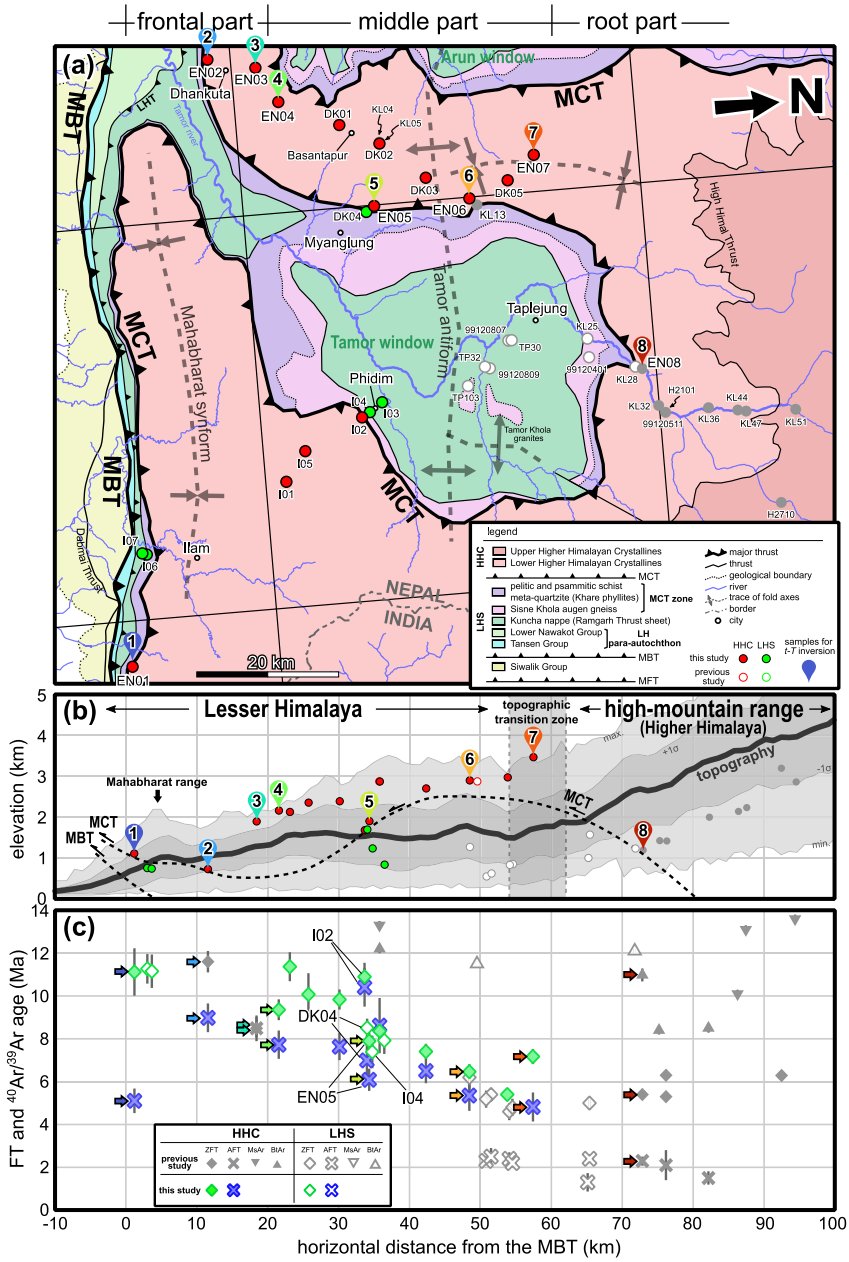

Figure 5. (a) The geologic map of eastern Nepal (see Figures 1a and 3 for location). Sample locations for the FT age dating (circles) and thermochronological inverse analyses (EN01–08: pins) are shown in the map. Locations of samples reported by previous studies (Larson et al., 2017; Sakai et al., 2017; Sakai, Iwano, Danhara, Takigami, et al., 2013) are also shown. The geologic map was modified after Sakai, Iwano, Danhara, Takigami, et al. (2013), Schelling and Arita (1991), and Mahato (2011). (b) The average topography of the study area along the across-strike section. Broken lines represent the approximate position of the Main Central Thrust and the Main Boundary Track. Sample locations are also projected on the cross-section. (c) The across-strike distribution of the zircon fission track and apatite fission track ages from this study, Larson et al. (2017), Sakai, Iwano, Danhara, Takigami, et al. (2013), and Sakai et al. (2017). Sample localities of these dated samples are projected perpendicularly onto the N5°E line. Arrows denote the FT ages used for thermochronological inverse analysis. MsAr = muscovite $^{40}Ar/^{39}Ar$ age; BtMr = biotite $^{40}Ar/^{39}Ar$ age.

low-grade metamorphic rocks of the Taplejung Group (Schelling, 1992; Schelling & Arita, 1991; Shrestha et al., 1984) and is exposed in the southern part of the study area and in the Tamor window. In the central part of the Tamor window around the Tamor antiform axis (Figure 5a), the Taplejung Group is intruded by the Proterozoic granite of Tamor Khola granites (Sakai, Iwano, Danhara, Takigami, et al., 2013; Shrestha et al., 1984).

The Lesser Himalayan Duplex has not been observed in the Tamor window. The MCT zone consists of mylonitic augen gneiss (the Sisne Khola augen gneiss), meta-quartzite, pelitic schist, and amphibolite (the Khare phyllites: Schelling, 1992). The MCT zone displays an inverted metamorphic sequence: metamorphic grade increases from the biotite-zone through the garnet-zone (ca. 550–575°C) at the bottom of the MCT zone, and to the kyanite-zone (ca. 610°C) at the top (Groppo et al., 2009; Imayama et al., 2010; Kawakami et al., 2019).

The timing of the initiation of the MBT movement is not constrained in the Central Himalaya. Some studies suggest that the cessation of the MCT activity was at ca. 12–10 Ma, hence the formation of MBT probably post-dated it (DeCelles et al., 2001; Meigs et al., 1995). The initiation of the MFT activity is suggested to be older than ca. 40 Ka based on the luminescence dating of the fault gouge (Mukul et al., 2007). The MBT and the MFT steeply dip (~60°) toward the NNE at the surface, and they are considered to root into a low-angle decollement located at ~6 km depth (Schelling & Arita, 1991). The geometry of the MHT at the upper- and middle-crustal depths has not been constrained by seismic and geodetic studies in eastern Nepal.

3. Reconstruction of *t-T* Path by Inverse Analysis of Fission-Track Data

3.1. Methodology

3.1.1. Data Collection

A total of 17 rock samples were collected from the HHC nappe and the LHS in eastern Nepal (Figures 5a and 5b, and Table 1) for FT dating of zircon and apatite. Three additional rock samples (EN02, EN03, EN08) collected by previous studies (Sakai, Iwano, Danhara, Takigami, et al., 2013; Sakai et al., 2017) and FT data from them were also used in this study (Table 5). For these samples, we incorporated new FT length data for thermochronological inverse analysis. Descriptions of rock samples used in the FT dating are given in Supplementary material A. Details of FT age determination and FT length measurement are reported in Supplementary material B.

In the Himalayas, a growing number of zircon and apatite (U–Th–Sm)/He ages, as well as FT ages, are available (Carrapa et al., 2016; Coutand et al., 2014; DeCelles et al., 2020; Ghoshal et al., 2020; Herman et al., 2010; Landry et al., 2016; Schultz et al., 2017). In recent years, however, several studies have pointed out that the diffusion of He in zircon and apatite is significantly affected by radioactive damages accommodated in the crystal lattice of these minerals, and models considering this effect are required for reliable interpretation of (U–Th–Sm)/He ages (e.g., Green & Duddy, 2018). Protolith ages of the HHC and LHS are quite old (mainly composed of the Precambrian: e.g., Parrish & Hodges, 1996), and the effects of the radiation damage cannot be ignored in geochronological interpreting the (U–Th–Sm)/He data. The impact of the radiation damage is probably small in much of the rapidly cooled geotectonic units, however, the geological background and cooling history of individual samples and thermochronometer should be carefully considered for interpretation of the published (U–Th–Sm)/He data (Whipp et al., 2022). Consequently, we exclude the published (U–Th–Sm)/He ages and focus on FT ages in this study.

3.1.2. Thermochronological Inverse Analysis

Thermochronological inverse analysis based on the FT annealing models was carried out for both ZFT and AFT data to constrain the *t-T* path at the wide temperature range from 350 to 60°C. The inversion was performed on eight samples (Table 1) from which ZFT age, ZFT length, AFT age, and AFT length data were fully available. Following the recommendation by Yamada, Takami, Nishimura (1995) and Yamada, Takami, Nishimura, Ito (1995), only the ZFTs that intersect with the zircon *c*-axis in high angles (>60°) were used for the thermochronological inverse analysis.

Modeling parameters and data used are summarized in Table 2. The Monte Carlo approach was used in searching for an adequately-fitting solution among the candidate *t-T* paths. The modeled FT age and FT length distribution calculated from randomly-generated *t-T* paths were evaluated by the Kolmogorov-Smirnov test. The inverse calculation was performed using the computer program HeFTy version 1.9.3 (Ketcham, 2005). The fanning curvilinear models (ZFT: Ketcham, 2019; AFT: Ketcham et al., 2007) were adopted for the FT age and FT length forward calculation. The threshold of the Kolmogorov-Smirnov test was set at $p = 0.5$ ("good" path) and $p = 0.05$ ("acceptable" path), and random trials were repeated until 100 "good" paths were accumulated. The "goodness-of-fit product weighted mean" of the "good" and "acceptable" paths (Ketcham, 2005) were eventually adopted as a thermal history, and error areas were represented by the range of "good" and "acceptable" paths.

Table 1
Summary of Rock Samples Used for FT Analyses

Sample no.	E (deg)	N lat. (deg)	d_{MBT}[a] (km)	Elevation (m)	Rock type	Formation	ZFT age	ZFT length	AFT age	AFT length	*t*-T inversion	References
EN01	88.0585	26.8096	1.2	1,108	Garnet two-mica gneiss	Junbesi Paragneiss (immediate hangingwall of MCT)	✓	✓	✓	✓	✓	
EN02	87.3066	26.9719	11.6	727	Garnet two-mica gneiss	Junbesi Paragneiss (immediate hangingwall of MCT)	✓	✓	✓	✓	✓	Sakai et al. (2017)
EN03	87.3153	27.0328	18.4	1,896	Biotite gneiss	Junbesi Paragneiss (~2 km above MCT)	✓	✓	✓	✓	✓	Sakai et al. (2017)
EN04	87.3670	27.0563	21.6	2,161	Garnet two-mica gneiss	Junbesi Paragneiss (~2 km above MCT)	✓	✓	✓	✓	✓	
EN05	87.5115	27.1578	34.3	1,902	Garnet two-mica gneiss	Junbesi Paragneiss (immediate hangingwall of MCT)	✓	✓	✓	✓	✓	
EN06	87.5076	27.2853	48.4	2,899	Garnet two-mica gneiss	Junbesi Paragneiss (immediate hangingwall of MCT)	✓	✓	✓	✓	✓	
EN07	87.4598	27.3704	57.4	3,467	Garnet-kyanite-biotite gneiss	Junbesi Paragneiss (~4 km above MCT)	✓	✓	✓	✓	✓	
EN08	87.7387	27.4839	72.8	1,195	Garnet two-mica gneiss	Junbesi Paragneiss (immediate hangingwall of MCT)	✓	✓	✓	✓	✓	Sakai, Iwano, Danhara, Takigami, et al. (2013)
I01	87.8432	27.0267	23.1	2,128	Garnet-biotite gneiss	Junbesi Paragneiss	✓					
I02	87.7704	27.1282	33.7	1,682	Garnet-sillimanite-biotite gneiss	Junbesi Paragneiss (immediate hangingwall of MCT)	✓		✓			
I03	87.7536	27.1549	36.4	838	Metaquartzite	Fagfog Quartzite	✓					
I04	87.7647	27.1385	34.7	1,234	Garnet two-mica schist	Khare phyllites	✓					
I05	87.8068	27.0536	25.7	2,355	Sillimanite-biotite gneiss	Junbesi Paragneiss	✓					
I06	87.9196	26.8444	3.6	741	Two-mica schist	Khare phyllites	✓					
I07	87.9177	26.8390	3.0	753	Foliated granite	Sisne Khola augen gneisses	✓					
DK01	87.4022	27.1302	30.1	2,389	Garnet two-mica gneiss	Junbesi Paragneiss (~2 km above MCT)	✓	✓	✓			
DK02	87.4296	27.1785	35.8	2,871	Garnet-kyanite-biotite gneiss	Junbesi Paragneiss (~3 km above MCT)	✓	✓	✓			
DK03	87.4772	27.2329	42.3	2,702	Garnet two-mica gneiss	Junbesi Paragneiss	✓		✓			
DK04	87.5138	27.1549	34.0	1,696	Mylonitic granite	Sisne Khola augen gneisses	✓	✓	✓			
DK05	87.4889	27.3351	53.8	2,973	Garnet-kyanite two-mica gneiss	Junbesi Paragneiss	✓					

[a]Horizontal distance from the suface trace of the MBT. Sample locations are perpendicularly projected onto the N5°E line.

In the inverse calculation, the initial conditions for temperature and time were set as 346.7–477.5°C and 21.0–8.2 Ma, respectively, based on the $^{40}Ar/^{39}Ar$ constraints. The temperature range was given based on the partial retention zone of muscovite $^{40}Ar/^{39}Ar$ system under which 10%–90% of ^{40}Ar is retained for 10^6–10^7 yr (Hames & Bowring, 1994). However, for most of the samples, due to poor availability of $^{40}Ar/^{39}Ar$ data from the same or nearby samples, the range of maximum and minimum muscovite $^{40}Ar/^{39}Ar$ age reported in eastern Nepal (21.0 and 8.2 Ma: Larson et al., 2017; Sakai, Iwano, Danhara, Takami, 2013) was used for the time constraint. Because of the low-reliability of the reconstructed *t-T* path in the temperature range above PAZ of ZFT, the results in this temperature range were excluded for constructing the thermal history. In the case of sample EN08, reliable muscovite $^{40}Ar/^{39}Ar$ plateau age of 11.0 ± 0.3 Ma (Sakai, Iwano, Danhara, Takami, et al., 2013) was used as the initial condition for the inverse calculation of this sample.

3.2. Results of FT Measurements

The results of the ZFT and AFT dating are summarized in Tables 3 and 4. The central and weighted average ages are also shown for reference. The pooled ages of the secondary standards confirm the reproducibility of the

Table 2
Thermochronological Inverse Analysis Model Parameters

Thermochronological data		Sample name		References
ZFT and AFT data used		EN02	ZFT data	Sakai et al. (2017)
		EN03	ZFT, AFT data	Sakai et al. (2017)
		EN08	ZFT, AFT data	Sakai, Iwano, Danhara, Takigami, et al. (2013)
		Others	ZFT, ZFTL, AFT, AFTL data	This study
Initial condition				**References**
Present surface temperature		15°C-(elevation (km) × 0.6 (°C/km)) ± 15°C		Naito et al. (2006)
Initial constraint	Time	EN08	11.6–10.4 Ma	Sakai, Iwano, Danhara, Takigami, et al. (2013)
		Others	21.0–8.2 Ma	Range of muscovite $^{40}Ar/^{39}Ar$ cooling age in eastern Nepal (Larson et al., 2017; Sakai, Iwano, Danhara, Takigami, et al., 2013)
	Temp.		346.7–477.5°C	10–90% retention of Ar in 10^6–10^7 years (Hames & Bowring, 1994)
t-T path generation		Random generation of monotonic cooling scenario		
Model parameters				**References**
ZFT annealing model		Fanning curvilinear		Ketcham et al. (2007)
AFT annealing model		Fanning curvilinear		Ketcham et al. (2019)
GOF method		Kolmogorov-Smirnov test		
Threshold		"good"	$p = 0.5$	Ketcham (2005)
		"acceptable"	$p = 0.05$	Ketcham (2005)
Ending Condition		until 100 "good" paths found		

measurements. The radial plots and kernel density estimates are shown in Figures S-C1 and S-C2 of Supporting Information S1 as a reference for homogeneity of grain ages.

3.2.1. ZFT Age and Length

A total of 17 new ZFT ages were obtained from the HHC nappe and underlying LHS distributed in eastern Nepal (Table 3, Figure 5). The ZFT ages from the HHC nappe range from 5.4 ± 0.3 Ma (DK05) to 11.4 ± 0.7 Ma (I01). The ZFT ages from the LHS range from 7.4 ± 0.8 Ma (I04) to 11.3 ± 0.7 Ma (I07). The significant age gap between two samples bounded by the MCT (I02 and I04) is recognized in the southern limb of the Tamor window, whereas the gap is not significant in the middle part of the HHC nappe (between EN05 and DK04). The age gap is not recognized in the northern limb of the Tamor window (Sakai, Iwano, Danhara, Takigami, et al., 2013).

The average ZFT lengths range from 9.9 to 10.4 μm. In all samples, the average lengths are significantly shorter than the initial track length (~10.5–11.0 μm: Hasebe et al., 1994; Yamada, Takami, & Nishimura, 1995). All the ZFT length distributions show a non-Gaussian distribution except for EN03 (Figure 6b-3), indicating that the partial annealing of the ZFT has occurred.

3.2.2. AFT Age and Length

11 AFT ages newly obtained from the HHC nappe and LHS (Table 4) show a unimodal age distribution (Figure S-C2 in Supporting Information S1), and range from 4.8 ± 0.7 Ma (EN07) to 10.4 ± 0.9 Ma (I02). The HHC nappe and the underlying LHS (samples DK04 and EN05) give similar AFT ages as in the case of the ZFT age (Figure 5c).

Table 3
Summary of ZFT Age Determinations Using LA–ICP–MS and ZFT Length Measurements

Sample no.	Mount no.	ZFT age determinations										ZFT length measurements			
		n	N_s	ρ_s	^{238}U(ppm)	FCT age (Ma)	±σ	$p(Q_{stat})$	Pooled age (Ma)	±σ	Central age (Ma)	±σ	Tracks*		ZFT length (μm)	±σ
EN01	1	26	1,578	3.9	871.3	27.4	2.7	0.42	**11.1**	**1.1**	11.2	0.4	201	(133)	**10.0**	**1.6**
EN04	1	26	914	1.6	411.5	27.5	1.2	0.00	**9.4**	**0.5**	9.4	0.5	138	(78)	**10.4**	**1.5**
EN05	1	29	2,152	2.6	721.6	27.3	1.3	0.00	**7.9**	**0.4**	8.1	0.3	197	(121)	**10.0**	**1.8**
EN06	1	29	1,661	2.5	788.9	27.3	1.3	0.00	**6.5**	**0.3**	7.1	0.4	206	(149)	**10.2**	**1.2**
EN07	1	28	2,488	3.3	956.1	27.3	1.3	0.00	**7.2**	**0.4**	7.3	0.3	192	(132)	**10.0**	**1.6**
I01	1	27	1,321	3.1	609.2	28.3	1.6	0.19	**11.4**	**0.7**	11.5	0.4				
I02	1	25	1,269	3.5	738.3	28.3	1.6	0.00	**10.9**	**0.7**	11.2	0.6				
I03	1	28	264	1.2	335.8	26.6	1.5	0.05	**7.9**	**0.6**	8.5	0.7				
I04	1	27	713	2.2	722.4	27.4	2.7	0.76	**7.4**	**0.8**	7.5	0.3				
I05	1	30	2,183	2.7	687.2	27.4	2.7	0.16	**10.1**	**1.0**	10.2	0.3				
I06	1	28	421	3.9	796.3	26.6	1.5	0.05	**11.2**	**0.8**	11.9	0.7				
I07	1	28	776	4.1	792.9	26.6	1.5	0.00	**11.3**	**0.7**	11.8	0.6				
DK01	1	28	1,482	2.0	493.9	27.5	1.2	0.18	**9.8**	**0.5**	9.9	0.3	76	(53)	**9.9**	**1.7**
DK02	1	28	1,218	2.1	645.4	28.1	1.3	0.06	**8.4**	**0.4**	8.5	0.3	102	(69)	**9.9**	**1.8**
DK03	1	25	1,211	2.1	675.0	27.5	1.2	0.00	**7.5**	**0.4**	7.5	0.4				
DK04	1	27	2,043	2.3	530.1	27.3	1.3	0.08	**8.5**	**0.4**	8.6	0.2	81	(54)	**10.0**	**1.6**
DK05	1	25	1,542	3.1	1162.1	27.3	1.3	0.00	**5.4**	**0.3**	5.5	0.3				

Note. n = number of grains, N_s = number of spontaneous fission track, ρ_s = spontaneous fission track density, ^{238}U = pooled mean concentration of uranium-238, FCT age (Ma) = pooled FT age of the Fish Canyon Tuff zircon (reference age of 28.4 Ma: Gleadow et al. [2015]) calculated based on ζ value of each samples, $p(Q_{stat})$ = the p-value of a Chi-square probability for homogeneity, tracks* = a number of all measured confined tracks and a number of the confined tracks with the crystallographic c-axis angles >60°. These bold ages are adopted for cooling age in this study.

Table 4
Summary of AFT Age Determinations Using LA–ICP–MS and AFT Length Measurements

Sample no.	Mount no.	AFT age determinations											AFT length measurements				
		n	N_s	ρ_s	^{238}U(ppm)	Durango apatite (Ma)	±σ	$p(Q_{stat})$	Pooled age (Ma)	±σ	Central age (Ma)	±σ	Tracks	AFT length (μm)	±σ	D_{par} (μm)	±σ
EN01	1	29	114	0.1	24.6	31.7	2.5	0.9	**5.1**	**0.6**	5.6	0.5	64	**10.9**	**2.5**	1.8	0.2
EN02	1	29	181	0.1	27.4	31.2	2.9	0.7	**8.3**	**0.8**	9.0	0.7	60	**12.9**	**2.4**	1.6	0.2
EN04	1	25	421	0.3	69.0	30.5	2.9	0.5	**7.7**	**0.7**	8.0	0.4	92	**12.4**	**1.8**	1.3	0.2
EN05	1	31	431	0.2	56.2	31.2	2.9	1.0	**6.1**	**0.5**	6.2	0.3	118	**13.3**	**2.1**	1.8	0.2
EN06	1	26	82	0.1	31.4	30.7	2.9	1.0	**5.3**	**0.7**	5.6	0.6	120	**13.4**	**1.8**	1.6	0.3
EN07	2	28	68	0.1	23.1	31.2	2.9	1.0	**4.8**	**0.7**	5.4	0.7	37	**12.7**	**1.9**	1.6	0.2
I02	1	28	278	0.1	21.2	31.7	2.5	0.7	**10.4**	**0.9**	10.9	0.7					
DK01	1	29	555	0.2	46.1	30.5	2.9	0.6	**7.6**	**0.6**	7.9	0.4					
DK02	2	24	90	0.1	11.0	30.1	2.7	1.0	**8.6**	**1.3**	9.3	1.0	58	**12.8**	**2.3**	1.8	0.4
	4	16	56	0.1	13.6	31.0	2.5	1.0	**8.9**	**1.6**							
DK03	1	30	369	0.1	37.5	30.5	2.9	1.0	**6.5**	**0.6**	6.8	0.4					
DK04	1	29	41	0.03	7.8	30.2	4.8	1.0	**7.0**	**1.1**	8.7	1.3					

Note. n = number of grains, N_s = number of spontaneous fission track, ρ_s = spontaneous fission track density, ^{238}U = pooled mean concentration of uranium-238, Durango apatite (Ma) = pooled FT age of the Durango apatite (reference age of 31.4 Ma: Green, 1985) calculated based on ζ value of each samples, $p(Q_{stat})$ = the p-value of a Chi-square probability for homogeneity, These bold ages are adopted for cooling age in this study.

Table 5
Summary of ZFT and AFT Data Reported by Previous Studies

Sample No.	Mineral	n	Spontaneous N_s	Spontaneous ρ_s	Induced N_i	Induced ρ_i	Dosimetry N_d	Dosimetry ρ_d	ζ_{MS}	$\pm\sigma$	$p(Q_{stat})$	Pooled age (Ma)	$\pm\sigma$	FT length measurements (this study): Tracks	FT length (μm)	$\pm\sigma$	D_{par} (μm)	$\pm\sigma$	References
EN02	Zircon	29	1,233	2.9	1,869	4.4	4,203	10.0	351	6	0.12	**11.6**	**0.5**	143 (91)	**9.8**	**1.4**			Sakai et al. (2017)
EN03	Zircon	30	1,990	2.2	3,601	4.0	3,768	7.9	390	3	1.00	**8.5**	**0.3**	102 (61)	**10.6**	**1.2**			Sakai et al. (2017)
EN03	Apatite	30	414	1.3	5,965	1.9	3,940	8.2	300	4	0.98	**8.5**	**0.5**	100	**13.6**	**1.9**	1.6	0.2	Sakai et al. (2017)
EN08	Zircon	30	957	2.4	2,485	0.6	3,763	7.4	380	3	0.31	**5.4**	**0.4**	131 (84)	**10.2**	**1.0**			Sakai, Iwano, Danhara, Takigami, et al. (2013)
EN08	Apatite	50	102	2.5	7,175	1.8	3,966	99.2	321	4	0.91	**2.3**	**0.2**	41	**12.9**	**2.0**	1.7	0.4	Sakai, Iwano, Danhara, Takigami, et al. (2013)

Note. n = number of grains, N_s = number of spontaneous fission track, ρ_s = spontaneous fission track density, N_i = number of induced fission track, ρ_i = induced fission track density, N_d = number of induced fission track in external detector adjacent to dosimeter, ρ_d = induced fission track density in external detector adjacent to dosimeter, ζ_{MS} = published calibration factors (Danhara et al., 2003, 2007), $p(Q_{stat})$ = the p-value of a Chi-square probability for homogeneity.

The average AFT lengths are ~12–13 μm (Figure 6c), with the majority of horizontal confined tracks shorter than the initial AFT length (~16 μm: Ketcham et al., 2015). The average length for sample EN01 was 10.9 ± 2.5 μm, which is much shorter than the length obtained from other samples (Figure 6c-1).

3.2.3. FT Age Distribution Pattern

Figure 5c summarizes the across-strike distribution of newly-obtained and published ZFT, AFT, and $^{40}Ar/^{39}Ar$ mica ages (Imayama et al., 2012; Larson et al., 2017; Sakai, Iwano, Danhara, Hirata, et al., 2013; Sakai et al., 2017). Samples collected from the frontmost part of the HHC nappe and the LHS yielded the ZFT age of ca. 11 Ma (Figure 5c). The ZFT ages are roughly constant from 1 to 10 km north of the MBT, and then progressively decrease toward the north (~60 km north from the MBT). In the southern slope of the high-mountain range (~60–100 km north from the MBT), they again show constant values of ca. 6 Ma. The youngest ZFT age is obtained from the northern limb of the Tamor window (4.6 Ma: Sakai, Iwano, Danhara, Hirata, et al., 2013). As mentioned above, no significant FT age gap is recognized between the HHC nappe and the LHS, except for the gap observed between samples I02 and I04. Nakajima et al. (2020a, 2020b) reported a similar overall northward-younging trend of the ZFT ages from western-central Nepal and eastern-central Nepal.

The AFT ages also show the overall, northward-younging trend except for the Pliocene AFT age obtained from the frontmost part of the HHC nappe (Figure 5c). The AFT ages get significantly older toward the north at the frontal part of the HHC nappe, and then monotonously younger toward the northern part of the Tamor window (Figure 5c). The youngest AFT age is reported from the MCT zone (1.3 Ma: Larson et al., 2017), and ages are roughly constant in the Tamor window and the southern slope of the high-mountain range. Similar young AFT age at the frontmost part of the HHC nappe is observed in far-western Nepal, western-central Nepal, and Bhutan (Coutand et al., 2014; DeCelles et al., 2020), while it is not observed in central Nepal and Sikkim (Landry et al., 2016; Robert et al., 2009).

3.3. Results of Thermochronological Inverse Analysis

Figures 6 and 7 summarize the results of ZFT-AFT multi-system inversion. The reconstructed t-T paths of 8 samples displays stepwise cooling, which can be divided into rapid and gradual cooling phases. Especially, t-T paths of the samples from the middle part of the HHC nappe in the N-S section (EN04–07) can be divided into three cooling phases; first slow cooling (30–50°C/Myr), followed by rapid cooling (150–200°C/Myr) in the PAZ of ZFT, and final gradual cooling (<30°C/Myr) again in the PAZ of AFT (Figures 6a and 7). Such a t-T path

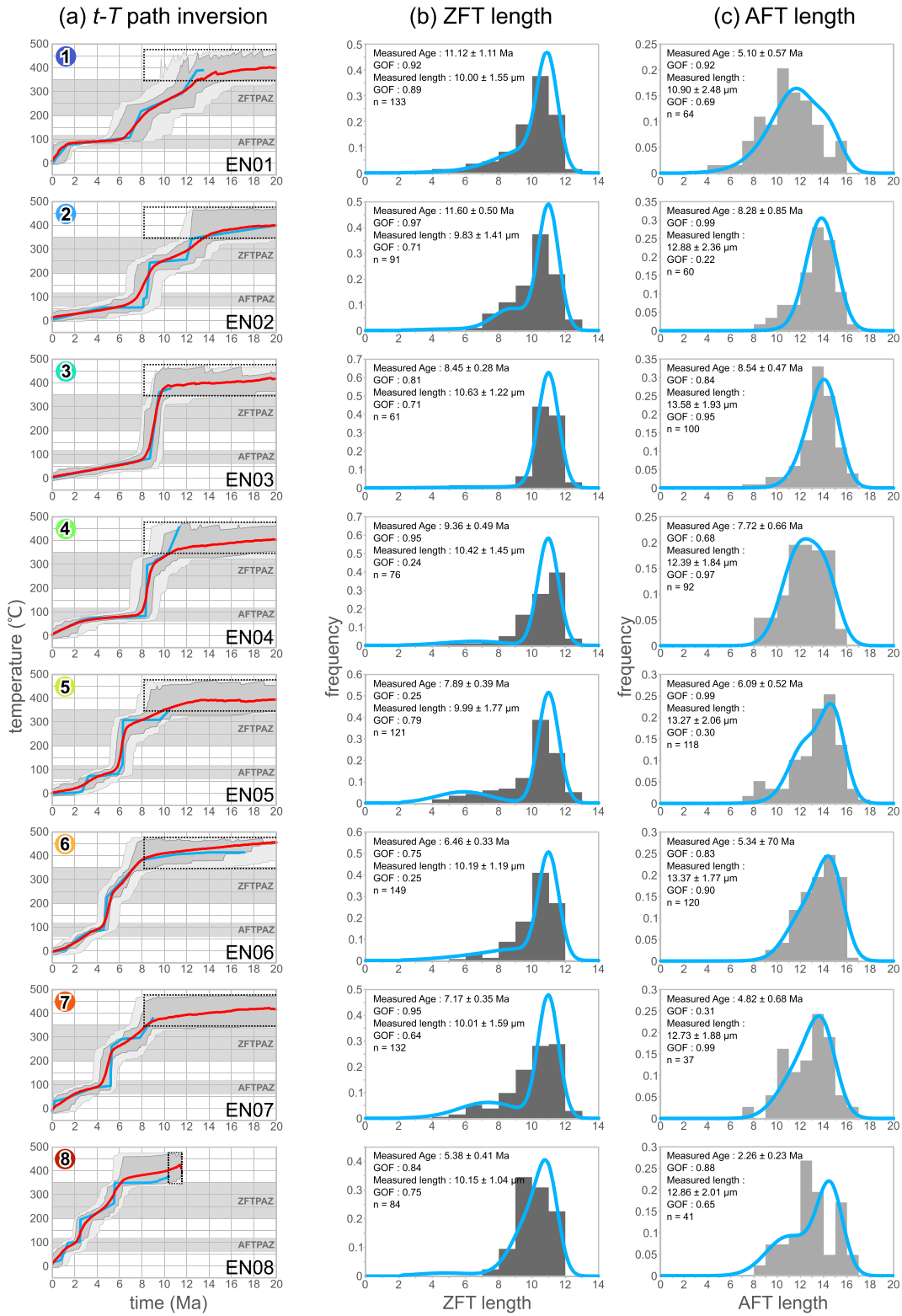

Figure 6. Results of thermochronological inverse analysis showing *t-T* paths calculated by HeFTy version 1.9.3 (Ketcham, 2005). (a) The solid sky-blue lines represent the best-fit path, and the solid red line indicates the weighted mean path. The dark gray and gray fields represent the "good" path ($p > 0.5$) and the "acceptable" path ($p > 0.05$) envelopes. The dotted rectangles represent initial condition. (b and c) The histograms of the zircon fission track and apatite fission track lengths are shown in each row. The solid sky-blue lines overlaid on histograms indicate the best fit modeled result of the forward calculation. GOF = goodness-of-fit (Ketcham, 2005).

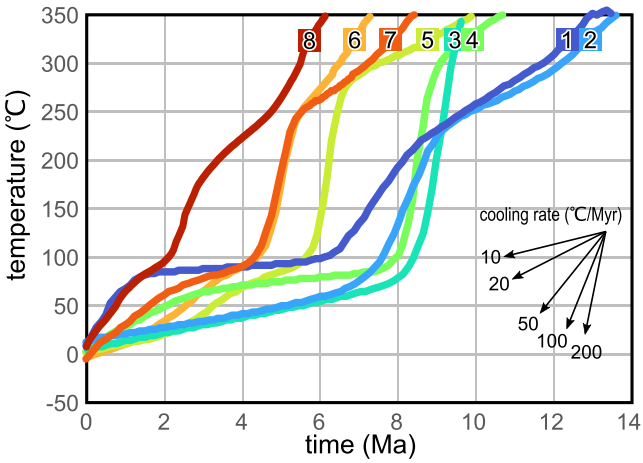

Figure 7. Weighted mean paths of the eight samples (show in in Figure 6a). Colors and numbers of each *t-T* path correspond to those of the location pins 1–8 shown in Figures 5a and 5b, and arrows in Figure 5c.

characterized by the gradual, rapid, and gradual cooling phases is termed "GRG cooling" in this study. For sample EN03, although gradual cooling in the high-temperature range is not seen, the cooling rate during the rapid cooling and following gradual cooling phases are similar to the four samples described above. The *t-T* paths of these five samples have a difference in the timing of the rapid cooling from 300°C to 100°C (Figures 6a-3 to 6a-7). It gradually becomes younger from south to north, that is, ca. 9 Ma (EN03), ca. 9–8 Ma (EN04), ca. 7–6 Ma (EN05), and ca. 5–4 Ma (EN06 and EN07). This northward-younging of the timing of the rapid cooling is the most remarkable and characteristic result of this study.

The *t-T* paths of the samples from the frontal part of the HHC nappe (EN01 and EN02) also show stepwise cooling, while the cooling is relatively than in the northern part (Figure 7). The *t-T* path of the sample from the frontmost part of the HHC nappe (EN01) shows a characteristic path: nearly constant gradual cooling (~30°C/Myr) from ca. 14 to ca. 6 Ma, followed by a constant-temperature period from ca. 6 Ma to ca. 2–1 Ma, and final rapid cooling (~60°C/Myr) in the latest stage (Figures 6a-1).

Sample EN08 is the only sample for which muscovite $^{40}Ar/^{39}Ar$ age (a plateau age of 10.98 ± 0.30 Ma: Sakai, Iwano, Danhara, Takigami, et al., 2013) and FT ages are both available, and thus likely yielded the most reliable thermal history above 350°C. The *t-T* path shows a two-step cooling, with the gradual cooling in the temperature range of the partial retention zone of muscovite $^{40}Ar/^{39}Ar$ system until ca. 6 Ma, followed by rapid cooling (Figures 6a-8). The fastest cooling rate was >100 °C/Myr, and the average cooling rate of the rapid cooling phase was ~60°C/Myr.

4. Thermokinematic Modeling

4.1. Thermokinematic Model Setup

In order to interpret the above-reported FT ages and *t-T* paths in the context of the denudation process, a 3-D thermokinematic modeling was performed. Forward calculations of FT ages and *t-T* paths were carried out using the finite element code of PECUBE (Braun, 2003; Braun et al., 2012). The parameters used for the 3-D thermokinematic model are summarized in Table 6. The 3-D crust model is created using a 40 km-thick crustal block coupled with the digital elevation model ("AW3D" global dataset derived from ALOS/PRISM, Japan Aerospace Exploration Agency) of the study area (118.5 × 264.8 km domain and 0.01-degree mesh: E87.2°–E88.4°; N26.6°–N29.0°: see also Figures S–D3 in Supporting Information S1). The rock transport velocity field **v** (*u, v, w*) is defined by a fault geometry and the original fault model of "PECUBE model" (available in PECUBE version 4.2.0) or the kink-band fault model (available in PECUBE version 3.0: Table 7 and Supplementary material D). The MHT strike angle is set to N85°W, and the mass transport direction is set perpendicular to the fault strike. Thermal field within the 3-D crust model is calculated by iterative solution of the 3-D advection-diffusion equation using the finite element method (Braun, 2003; Braun et al., 2012). The equation is generalized to include three advection terms as follows:

$$\frac{\partial T}{\partial t} + u\frac{\partial T}{\partial x} + v\frac{\partial T}{\partial y} + w\frac{\partial T}{\partial z} = \frac{\partial}{\partial x}\kappa\frac{\partial T}{\partial x} + \frac{\partial}{\partial y}\kappa\frac{\partial T}{\partial y} + \frac{\partial}{\partial z}\kappa\frac{\partial T}{\partial z} + A$$

where T is temperature, t is time, u, v, w are components of a general velocity field (**v**) determined from fault kinematics, κ is thermal diffusivity, and A is radiogenic heat production (Table 6). A *t-T* path of each sample is forwardly calculated from the modeled thermal field of each timestep and a particle path of the sample. The fanning curvilinear models (ZFT: Ketcham, 2019; AFT: Ketcham et al., 2007) are used for the forward calculation of a FT age from the modeled *t-T* path (Supplementary material F).

The thermokinematic model of this study assumes the following five conditions for simplification. First, the topography is assumed to be in steady state through the run time, and thermal influence on the cooling crust caused by the topographic growth is not taken into account. Previous studies pointed out that the upper crustal

Table 6
Summary of Thermokinematic Modeling Parameters

Parameters	Meaning	Values	Units	Reference
Mechanical parameters				
ρ_c	Crustal density	2,750	kg m^{-3}	
ρ_m	Mantle density	3,200	kg m^{-3}	
D	Crustal thickness	40	km	Schulte-Pelkum et al. (2005)
nx, ny, nz	Number of the grids	120, 260, 40		
E	Young modulus	100	GPa	
Thermal parameters				
K	Thermal conductivity	2.5	W m^{-1} K	Whipp et al. (2007)
κ	Thermal diffusivity	35.0	km^2 Myr^{-1}	
c	Specific heat capacity	800.0	J kg^{-1} K	Whipp et al. (2007)
A	Radiogenic heat production	1.6	μW m^{-3}	
T_b	Basal temperature	600.0–900.0	°C	
T_s	Surface temperature	15.0	°C	
L	Atmospheric lapse rate	6.0	°C km^{-1}	Naito et al. (2006)
Fault parameters				
v_o	Overthrusting velocity	6.0–33.0	mm yr^{-1}	
v_u	Underthrusting velocity	0.0–14.0	mm yr^{-1}	
v_{sf}	Overthrusting velocity of the hangingwall of the splay fault	0.0–12.0	mm yr^{-1}	

denudation in the Himalayas is primarily driven by tectonics, with topographic growth and climate as subordinate roles (Godard et al., 2014; Landry et al., 2016; van der Beek et al., 2016). Under this assumption, the exhumation rate can be defined as the vertical component (w) of a velocity field (**v**) of each surface mesh. In addition, most of the samples used in this study were collected from the N-S ridge line or from the southern hill slope. Therefore, the effect of an unrealistic exhumation pathway above the low-angled fault (Coutand et al., 2014) on the *t*-*T* path

Table 7
Summary of Kinematic Parameters Used for the Thermokinematic Models

		Flat MHT model			Flat-Ramp-Flat MHT model			Duplex 01 model		Duplex 02 model		Duplex 03 model		Splay fault model		
Fault model		PECUBE model			PECUBE model			Kink-band model		Kink-band model		Kink-band model		PECUBE model		
Fault		Initiation (Ma)	v_o (mm/yr)	v_u (mm/yr)	Initiation (Ma)	v_o (mm/yr)	vu (mm/yr)	Initiation (Ma)	v_o (mm/yr)	Initiation (Ma)	v_o (mm/yr)	Initiation (Ma)	vo (mm/yr)	Initiation (Ma)	v_o (mm/yr)	v_u (mm/yr)
	MCT	-	-	-	-	-	-	20.0	33.0	20.0	33.0	20.0	33.0	-	-	-
	RT	-	-	-	-	-	-	11.5	33.0	11.5	33.0	12.7	33.0	-	-	-
Duplex	D1	-	-	-	-	-	-	8.3	7.0	8.3	7.0	9.9	7.0	-	-	-
	D2	-	-	-	-	-	-	5.8	7.0	5.8	7.0	8.8	7.0	-	-	-
	D3	-	-	-	-	-	-	3.2	7.0	4.7	7.0	7.8	7.0	-	-	-
MHT	MBT	15.0	6.0–33.0	14.0	15.0	6.0	14.0	2.0	7.0	4.5	7.0	7.6	7.0	15.0	6.0	14.0
	DT	-	-	-	-	-	-	1.4	7.0	2.0	7.0	2.0	7.0	-	-	-
	MFT	-	-	-	-	-	-	0.8	7.0	0.8	7.0	0.8	7.0	-	-	-
Splay fault		-	-	-	-	-	-	-	-	-	-	-	-	2.0	0.0–12.0	0.0

and age prediction can be insignificant. Second, the forward model starts from a conductive steady state with no fault motion. We have no clear way of constraining paleo-geothermal field and must make assumptions at this point. In order to minimize the effect caused by the static steady-state initial condition, the forward models were calculated for 15 Myr, and only the data from 12 Ma to the present was accepted (Table 7). Third, shear heating accompanied by the slip of the MHT is not taken into account because numerical experiments estimated that the effective basal friction coefficient on the flat part of the MHT is smaller than 0.1 (Cattin & Avouac, 2000; Herman et al., 2010). Fourthly, we also do not consider the thermal perturbation caused by the growth of the Ama Drime horst (Figure 1a), a slip of the STD, and intrusion of the Miocene leucogranites (e.g., Leloup et al., 2010), because these are located farther north and distant enough to ignore their thermal influence on the study area. Finally, radioactive heat production is assumed to be constant during the run time and uniform throughout the modeled crust. All the *t-T* paths were obtained exclusively from the HHC nappe, and we do not address the cooling process of other geotectonic units. Although radioactive heat production is not a negligible parameter in estimating exhumation rates from *t-T* paths through inverse analysis, it can be simplified as a constant as in the present study when discussing systematic trends in *t-T* paths obtained by forward modeling (see also Supplementary material E).

Following four thermokinematic models were designed to test the published three tectono-thermal models proposed in the Central and Eastern Himalayas (the Overthrusting model, the Lesser Himalayan Duplex model, and the Out-of-Sequence Thrust model; Figures 4a–4c), and to constrain the primary factor that drove the denudation in eastern Nepal. The Lateral-Cooling model was excluded from the thermokinematic modeling because the tectonothermal processes are too complex to implement in the PECUBE model.

4.1.1. The Thermokinematic Models to Test the Overthrusting Model

4.1.1.1. The Flat MHT Model

The first model constructed in order to test the Overthrusting model is the "Flat MHT model" which assumes the MHT without the mid-crustal ramp. The geometry of the MHT is defined as a plane connecting the geophysically-determined shallow and deeper portions of the MHT as explained above (Figure 8a: Hauck et al., 1998; Schelling & Arita, 1991; Schulte-Pelkum et al., 2005). In this model, the MBT and the MFT are treated as a single fault located at the current surface trace of the MBT due to following two reasons: (a) the Quaternary activity of the MFT in this area has not been constrained because the surface trace of the MFT is obscure in eastern Nepal, (b) the FT age data are restricted to the hanging wall of the MBT and thus constraints on the Quaternary activity of the MFT is absent.

The convergence rate between model sides is set to 20.0 mm/yr based on the current convergence rate between the Indian and Eurasian plates (Ader et al., 2012; Bettinelli et al., 2006; Bilham et al., 1997; Lavé & Avouac, 2000; Mukul et al., 2010), and entire convergence partitions into the overthrusts of the hanging wall and underthrusting of the footwall of the MHT. The overthrusting rate (v_o) and underthrusting rate (v_u) of 6.0 and 14.0 mm/yr (Coutand et al., 2014; Herman et al., 2010; Robert et al., 2009, 2011; Whipp et al., 2007) are applied. In order to test whether a temporary increase in the v_o results in GRG cooling, two additional models in which v_o temporarily increases at 8–7 Ma ($v_{o(8\text{-}7)}$ = 18.0 and 33.0: Figure 8b center and right) are also constructed.

4.1.1.2. The Flat-Ramp-Flat MHT Model

A cross-section of the "Flat-Ramp-Flat MHT model" is portrayed in Figure 9a. Compared to the Flat MHT model described above, the geometry of the MHT alone is changed to the flat-ramp-flat one, and the mechanical, thermal, and fault parameters are kept unchanged. The cross-section proposed by Elliott et al. (2016) in central Nepal is extrapolated to the geometry of the MHT in eastern Nepal, and the dip angles of the flat and the mid-crustal ramp are set to 5° and 20°, respectively. The activity of the single thrust is associated with the denudation of the hanging wall, and its flat-ramp-flat geometry is assumed to be stable for 15 Myr (Figure 10). In this point, this model represents the same tectono-thermal process as the Overthrusting model (Coutand et al., 2014; Robert et al., 2009, 2011). We performed forward calculations with three basal temperature conditions (T_b = 600, 750, 900) in order to test the effect of basal temperature on the cooling process of the HHC nappe.

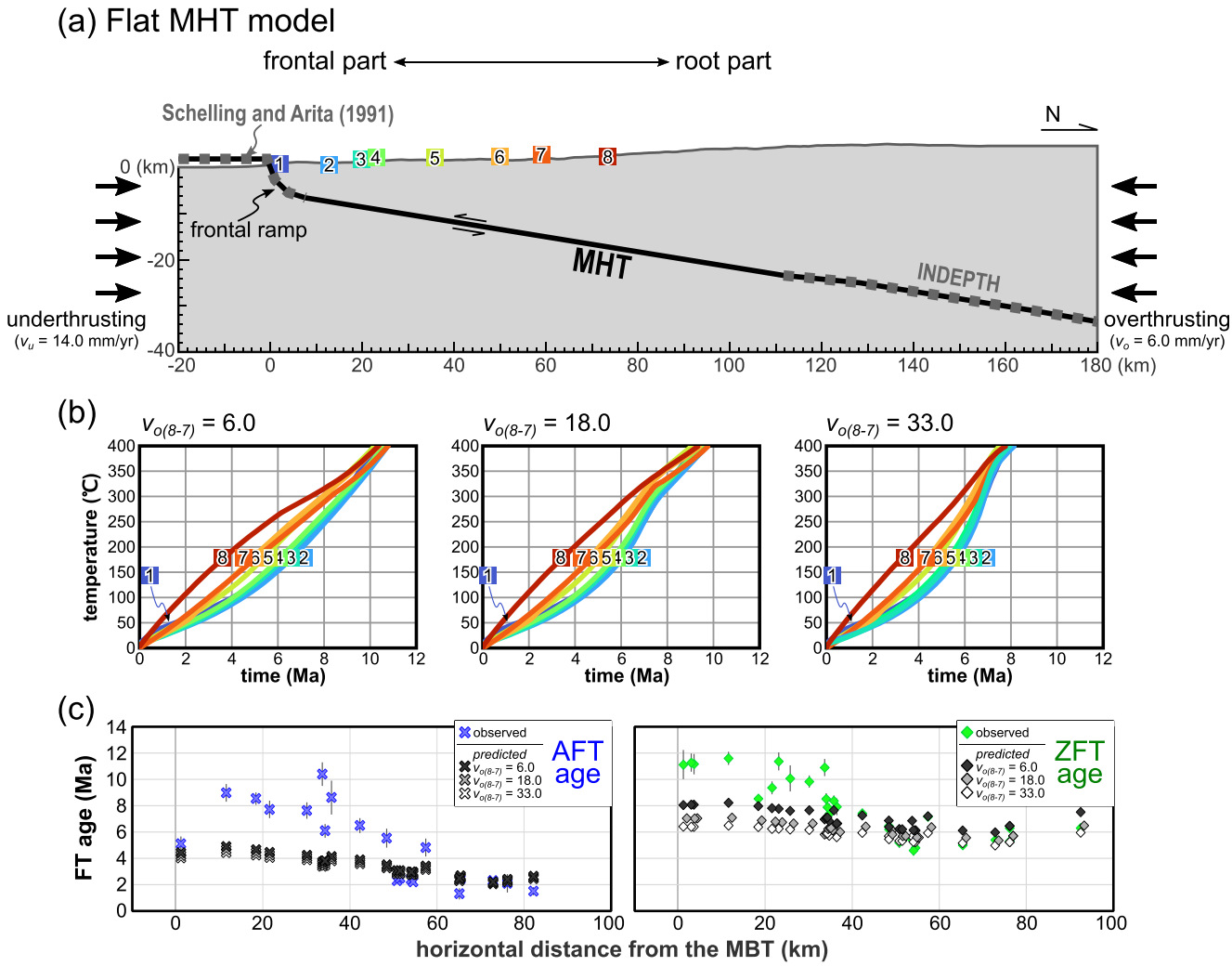

Figure 8. (a) Cross-section of the forward model geometry for the Flat Main Himalayan Thrust (MHT) model. The geometry of the MHT is determined by the combination of the balanced-cross section by Schelling and Arita (1991) (gray dotted part on the left side of the MHT), the INDEPTH Tib-1 reflection profile (Hauck et al., 1998) and the HIMNT profile (Schulte-Pelkum et al., 2005) (gray dotted part on the right side of the MHT), and a line connecting them. Numbered squares with various colors represent the locations of the samples used in the *t-T* forward modeling, which are perpendicularly projected onto the across-strike section. Colors and numbers of each sample localities correspond to those in (b) and those used to present the *t-T* inversion results (EN01–08) in Figures 5, 7 and 8. (b) The predicted *t-T* paths for the eight sampling points shown in (a) for $v_{o\ (8-7)}$ = 6.0 mm/yr (left), 18.0 mm/yr (center), and 33.0 mm/yr (right). (c) Results of the forward calculation of the apatite fission track ages (left) and the zircon fission track ages (right) for $v_{o\ (8-7)}$ = 6.0, 18.0, and 33.0 compared with the observed FT ages obtained from eastern Nepal (blue and green symbols).

4.1.2. The Duplex 01–03 Models to Test the Lesser Himalayan Duplex Model

These simple reference models aim to examine how the duplex growth affects the crustal thermal structure and the cooling process of the HHC nappe. In the study area, it is not certain whether the Lesser Himalayan Duplex lies just beneath the Tamor window. Hence, we extrapolated the balanced cross-sections proposed for other areas to the study area (Figure 11). We applied the balanced cross-section reported from central and western Nepal (DeCelles et al., 2020; Khanal & Robinson, 2013) for the following two reasons: (a) similarities in geological backgrounds (e.g., nappe and tectonic window are developed with a pair of syn- and antiform), (b) a relatively simple cross-section has been restored that can be simulated by PECUBE. The dip angle of the MHT along a flat is set to 5° and that along a ramp to 35°. Three thrust sheets with a thickness of ~5.4 km are designed to imbricate to form the hinterland dipping duplex (Figure 11d). A thinner thrust sheet corresponding to the Kuncha nappe (~2.3 km thick) overlies the duplex (DeCelles et al., 2020; Khanal & Robinson, 2013: Figures 11c and 11d). The across-strike position of the duplex is adjusted to be consistent with the position of the duplex-bending fold-axis

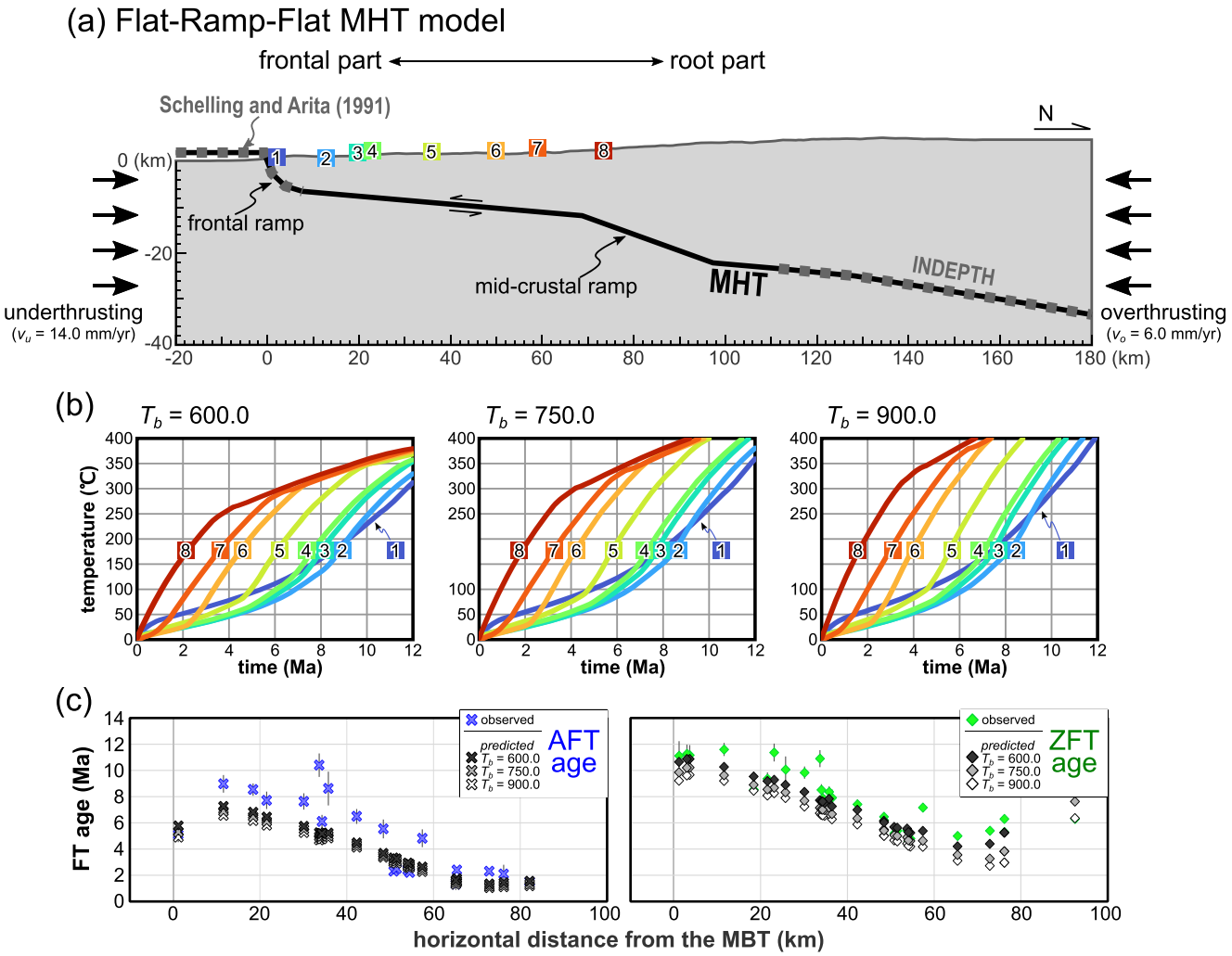

Figure 9. (a) Cross-section of the forward model geometry for the Flat-Ramp-Flat Main Himalayan Thrust (MHT) model. The geometry of the MHT is determined on the basis of a cross-section by Elliott et al. (2016) sandwiched by the geophysically constrained parts (gray dotted parts). (b) The predicted *t-T* paths for the eight sampling points shown in (a) for T_b = 600°C (left), 750°C (center), and 900°C (right). (c) Results of the forward calculation of the apatite fission track age (left) and the zircon fission track age (right) for T_b = 600, 750, and 900 compared with the FT ages observed in eastern Nepal.

and the Tamor antiform (Figure 11d). The duplex structure of the Siwalik sediments is designed based on a cross-section by Schelling and Arita (1991): the frontal edge of the MHT flat is set at 6 km depth. The MHT traces determined by the INDEPTH and HIMNT profiles (Hauck et al., 1998; Schulte-Pelkum et al., 2005) are not used to simplify the kinematic restoration. The full convergence is accommodated by the overthrusting of the hanging wall, thus the value of v_u is set to 0.0 throughout the run time (McQuarrie & Ehlers, 2015). The slip rates and duration times of the MCT, LHT, three thrusts on the duplex (D1–D3), MBT, Dabmai Thrust (DT), and MFT are set following Long et al. (2012) as summarized in Table 7. The kinematic sequence of this model is as follows: the HHC nappe is emplaced over the LHS rocks along the MCT, and the Kuncha and the HHC nappes are emplaced over the LHS rocks along the LHT at the rate of 33.0 mm/yr (Figure 11b and Table 7). Subsequently, accretion of the thrust sheets accompanying the slip of D1–D3 to form the Lesser Himalayan Duplex takes place (Figure 11c), which is followed by the slip of current MHT and sequential thrusting in the Siwalik sediments (Figure 11d).

After the 2015 M_w 7.8 Gorkha earthquake in central Nepal, geological studies (Ghoshal et al., 2020; Hubbard et al., 2016) proposed a balanced cross-section in which the mid-crustal ramp is located farther north than previously proposed (e.g., Khanal & Robinson, 2013). Hubbard et al. (2016) place the mid-crustal ramp just below an

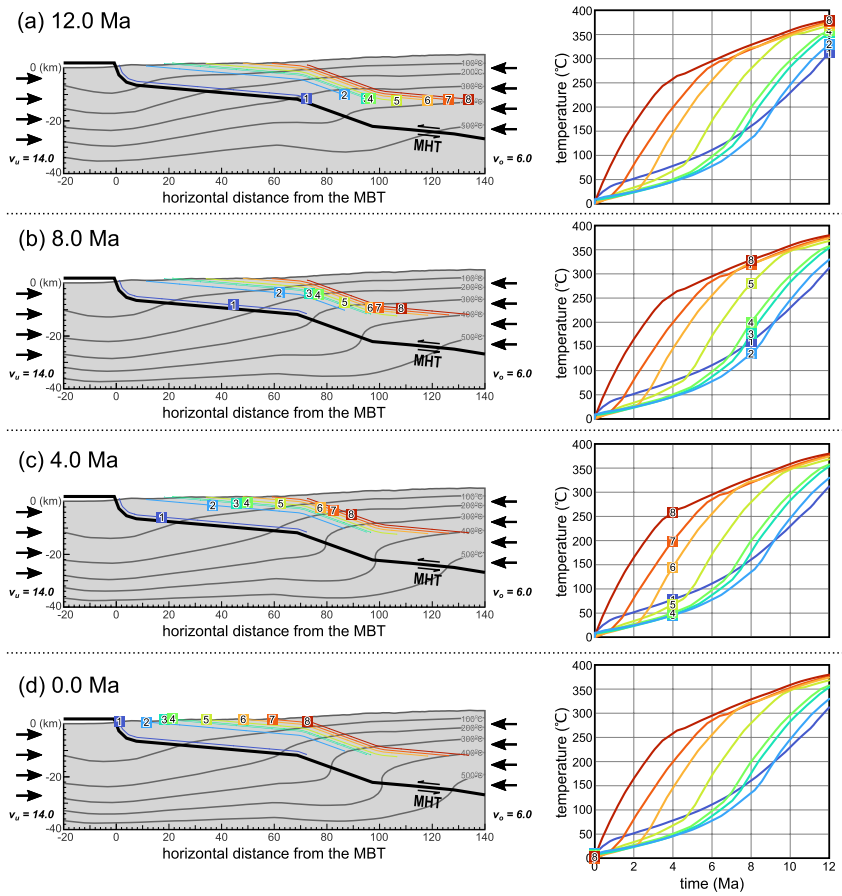

Figure 10. Sequentially restored kinematic scenarios for the Flat-Ramp-Flat Main Himalayan Thrust model (T_b = 600°C) and corresponding *t-T* path (Figures 11a and 11b) since 12 Ma. (a–d) Note that the particle paths and isotherms are projected onto the across-strike section, causing a slight deviation of the temperature in the cross-section from the *t-T* path of individual sample.

antiformal stacking duplex, and Ghoshal et al. (2020) restored a balanced cross-section with a ramp located at the northern edge of the duplex based on a cross-section by Whipple et al. (2016). Taking these studies into account, additional models varying the position of the mid-crustal ramp are constructed (the Duplex 02 and 03 models: Figure 12a center and right). These models exhibit the same geological structure at the present surface, however, the timing of growth of the duplex and antiform are different (Table 7). For instance, in the case of a ramp located at the frontal part of the duplex, the duplex must grow during 8.3–1.4 Ma (Figure 12a left; the Duplex 01 model). On the other hand, in the case of a ramp located at the northern edge of the duplex, the duplex must grow during 9.9–7.6 Ma (Figure 12a right; the Duplex 03 model).

4.1.3. The Splay Fault Model to Test the Out-of-Sequence Thrust Model

The Splay Fault model is shown in Figure 13a takes into account the out-of-sequence thrust activity of a splay fault since 2 Ma. The location of the mid-crustal ramp is at least 20 km north of the topographic transition zone in central Nepal (Whipple et al., 2016), which is significantly north of the locations in Robert et al. (2011) and Elliott et al. (2016). Hence, Whipple et al. (2016) explained that the building of the high-mountain range cannot be attributed to the steep uplifting above the mid-crustal ramp and that an out-of-sequence thrusting above the splay fault of the MHT fault imposed a first-order control on the rock uplift (Figures 4c and 13a). In the Nepalese Himalaya, geomorphic, cosmogenic nuclide, and thermochronological studies suggest that the Quaternary thrusting by such a hidden fault took place at the foot of the high-mountain range and that it has driven the rapid uplift of the high-mountain range since 2 Ma (Arita & Ganzawa, 1997; Blythe et al., 2007; Hodges et al., 2004; Wobus et al., 2003, 2006).

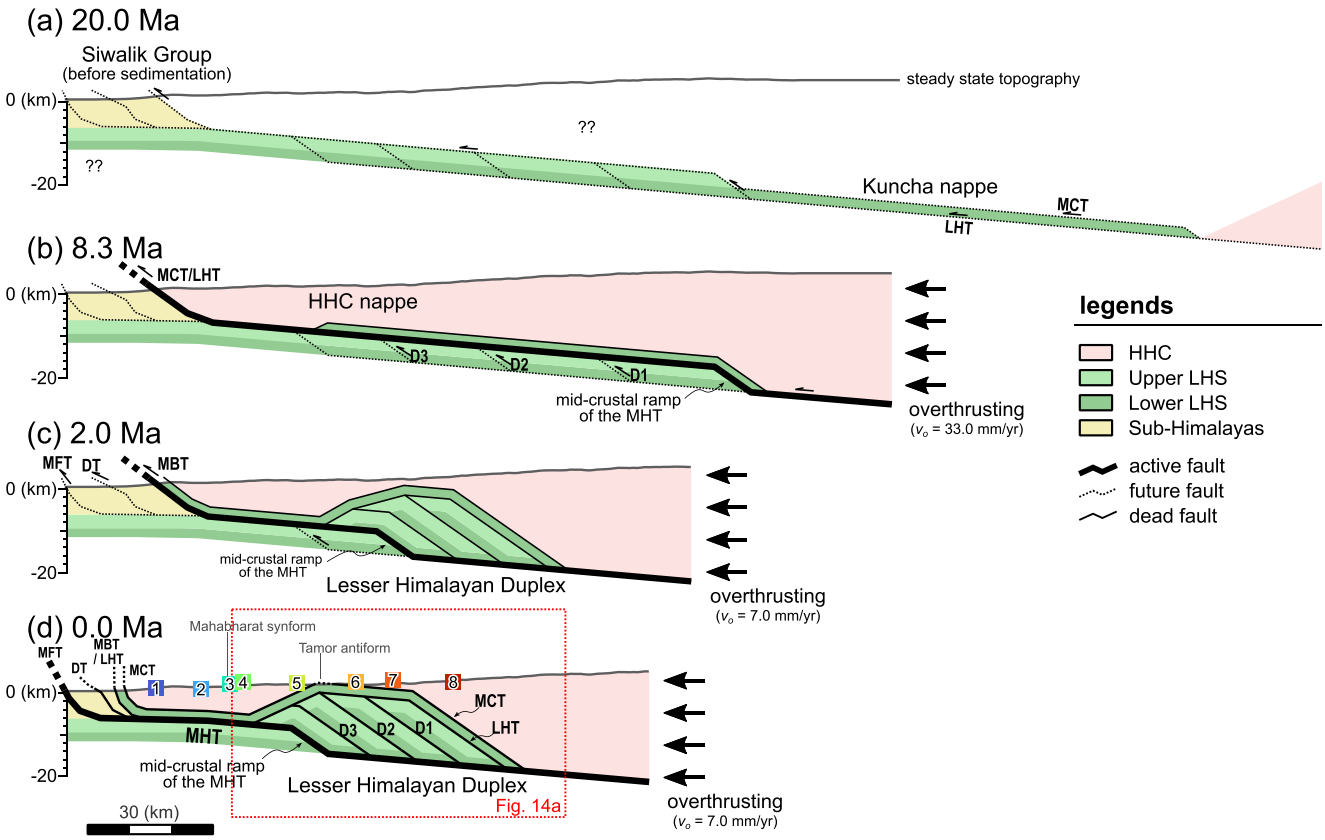

Figure 11. Sequentially-restored cross-sections illustrating the kinematic scenario for the Duplex 01 model. The scenario assumes constant shortening rates before (33.0 mm/yr) and after 8.3 Ma (7.0 mm/yr). (a) Initial cross-section at 20.0 Ma. (b) Cross-section just after the termination of the emplacement of the higher Himalayan crystalline and Kuncha nappe at 8.3 Ma. (c) Cross-section after the cessation of the D1–D3 thrust movements and the growth of the Lesser Himalayan Duplex at 2.0 Ma. (d) Final cross-section geometry after the activity of the Main Boundary Thrust, DT, and the Main Frontal Thrust rooting into the Main Himalayan Thrust. The hinterland-dipping duplex has developed beneath the Tamor antiform. Note that the crustal shortening progresses simultaneously with the deposition of the Siwalik Group in the foreland basin.

While splay fault activity has been pointed out in various areas of Nepal, the splay fault has not been recognized by field surveys in eastern Nepal. In this model, the location of the splay fault is adjusted to be consistent with the location of its assumed surface trace and the topographic transition zone in this area (Figure 13a). Therefore, samples EN07 and EN08 are interpreted as being located in the hanging wall of the splay fault. The overthrusting rate of the hanging wall of the splay fault is defined as a sum of v_o and v_{sf} in PECUBE model. Fault parameters (v_o, v_u, v_{sf}) used in the model are summarized in Table 7.

4.2. Results of the Forward Modeling of the *t-T* Paths and FT Ages

4.2.1. The Thermokinematic Models to Test the Overthrusting Model

4.2.1.1. The Flat MHT Model

The modeled *t-T* paths and FT ages for the Flat MHT model are shown in Figures 8b and 8c. The *t-T* paths for the eight sampling points show a roughly constant cooling rate (~40°C/Myr), and no significant difference in the cooling history is observed (Figure 8b left). The predicted FT age distribution is almost constant along the across-strike section (ZFT: ca. 8–6 Ma, AFT: ca. 5–2 Ma). In this model, the hanging wall of the MHT is uniformly uplifted, and the exhumation rate distribution is roughly constant along the section. Consequently, when the denudation of the HHC nappe is driven by the fault activity of the MHT, the cooling histories should resemble each other as long as the data are collected along the across-strike section. The modeled *t-T* paths and FT ages are inconsistent with the observed data in eastern Nepal (cf. Figures 5c and 8c).

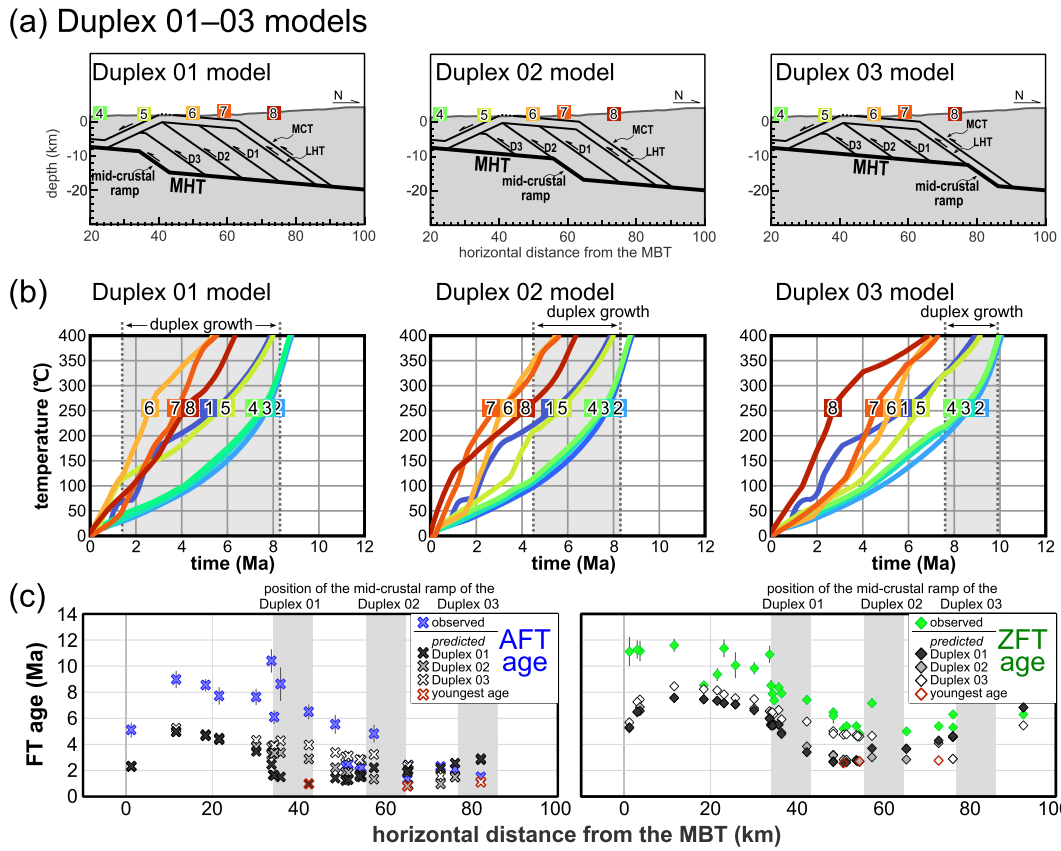

Figure 12. (a) Cross-section illustrating the geometries of the Duplex 01 model (left), Duplex 02 model (center), and Duplex 03 model (right). Note that the surface geometry of these models is the same, although the subsurface geometry of the Main Himalayan Thrust and the timings of the duplex growths are different (see also Table 7). (b) The predicted *t-T* paths for the eight sampling points shown in Figure 13d; left - Duplex 01 model, center - Duplex 02 model, right - Duplex 03 model. Gray-colored fields represent the timing of the duplex growths. (c) Results of the forward calculation (Duplex 01–03 models) of the apatite fission track ages (left) and zircon fission track ages (right) compared with the observed fission track ages in eastern Nepal.

This model confirms that a temporal change of v_o during ca. 8–7 Ma can result in GRG cooling (Figure 8b). If the overthrusting rate increased by a large margin during ca. 8–7 Ma ($v_{o(8\text{-}7)}$ = 33.0: Figure 8b right), then the cooling rate of the frontal part of the HHC nappe (paths 2–3) would also increase at ca. 7 Ma. These paths exhibit GRG cooling, whereas the samples from the middle and root parts yield approximately constant cooling paths. Temporal change of v_o does not significantly affect the ZFT and AFT age distribution patterns (Figure 8c).

4.2.1.2. The Flat-Ramp-Flat MHT Model

The modeled *t-T* paths and FT ages for the Flat-Ramp-Flat MHT model are shown in Figures 9b and 9c. The predicted FT age distribution patterns are notably consistent with the observed age patterns in eastern Nepal (Figure 9c): the modeled AFT ages are older toward the north at the frontal part (from ca. 8 Ma to ca. 6 Ma), and then monotonously younger toward the north (from ca. 8 Ma to ca. 1 Ma). The modeled ZFT ages are also consistent with observations in that they show a significant northward-younging trend with the oldest age (ca. 12 Ma) at the frontmost part and the youngest age (ca. 4 Ma) at the root part. Furthermore, Figure 9b shows that the predicted *t-T* paths have essentially the same character as the observed *t-T* paths in the following three points: (a) the *t-T* paths show stepwise cooling characterized by the rapid cooling phase at the temperature range of 350–150°C, and paths 4–7 show GRG cooling. (b) northward-younging of the timing of rapid cooling. (c) relatively slower cooling rate of path 1 compared to other *t-T* paths.

In this model, gradual and rapid cooling phases correspond to a low-angled uplift above the flat and a high-angled uplift above the ramp of the MHT, respectively. Figure 10 illustrates that the rock samples sequentially pass above

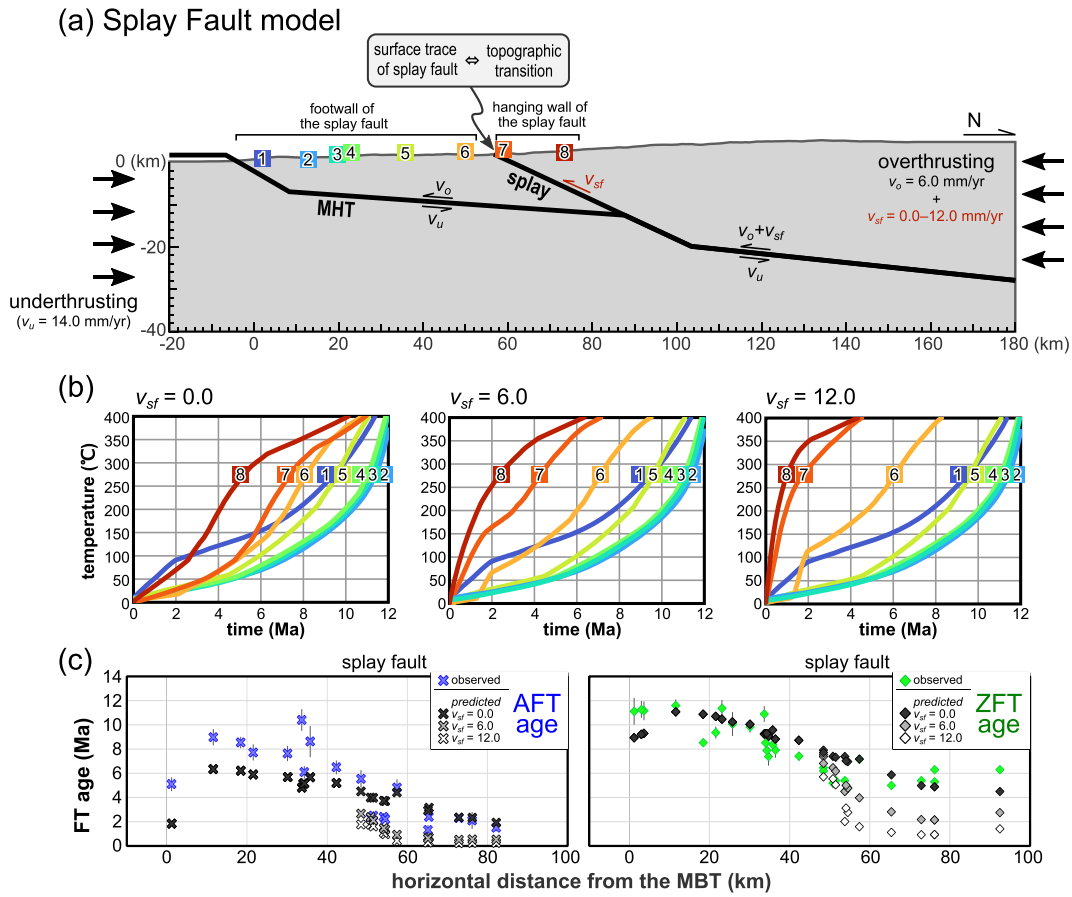

Figure 13. (a) Cross-section illustrating the geometry of the Splay Fault model. The location of the splay fault is adjusted to be consistent with the location of its surface trace and the topographic transition zone. Samples EN07 (path 7) and EN08 (path 8) are located in the hanging wall of the splay fault. (b) The predicted *t-T* paths for the eight sampling points shown in (a) for v_{sf} = 0.0 mm/yr (left), 6.0 mm/yr (center), and 12.0 mm/yr (right). (c) Results of the forward calculation of the apatite fission track ages (left) and the zircon fission track (ZFT) ages (right) for v_{sf} = 0.0, 6.0, and 12.0 compared with the observed FT ages in eastern Nepal.

the flat, ramp, and flat parts of the MHT during the southward-overthrusting process. They gradually cool down during the gentle uplift above the flat and rapidly cool down during the abrupt uplift above the ramp. Furthermore, the rock samples pass above the mid-crustal ramp sequentially from south to north as the hanging wall of the MHT moves southward, which results in northward-younging of the timing of the rapid cooling.

Variations in the basal temperature conditions (T_b = 600, 750, 900) did not yield any significant difference in the predicted FT ages and *t-T* paths at <300°C. At temperatures above 300°C, T_b = 600, 750 and 900°C yielded slightly different *t-T* paths: in the case of T_b = 600°C, rock samples gradually cooled at the temperature range of 300–400°C (Figure 9b left). In contrast, for higher-basal temperatures of T_b = 750 and 900°C, the gradual cooling phase appeared at a higher-temperature range (Figure 9b center and right).

4.2.2. The Duplex 01–03 Models to Test the Lesser Himalayan Duplex Model

The modeled *t-T* paths and FT ages for the Duplex 01–03 models are shown in Figures 12b and 12c. The predicted AFT and ZFT ages show concave-up age patterns above the duplex, with young FT ages at the frontmost part of the HHC nappe (Figure 12c). For the Duplex 01 model, the AFT ages are constant above the Lesser Himalayan Duplex, and the youngest AFT age is obtained above the current mid-crustal ramp at the southern edge of the duplex. For the Duplex 02 and 03 models, the AFT ages exhibit a northward-younging trend above the duplex,

and the location of the youngest AFT age corresponds to the current position of the mid-crustal ramp as in the case of the Duplex 01 model. Although some minor discrepancy exists between predicted and observed age values, the distribution pattern of model ages roughly reproduces the observed age distribution pattern. Considering the uncertainties associated with the FT ages, it may be difficult to distinguish these models by focusing solely on the FT age patterns. As can be seen in Figure 12b, however, the predicted *t-T* paths show remarkably different cooling processes between the three Duplex models. The predicted *t-T* paths of the Duplex 01 model do not exhibit GRG cooling and northward-younging of the timing of rapid cooling (Figure 12b left). The samples located above the duplex (samples EN06–08) cool down at a roughly constant, but faster rate than the other samples. This rapid cooling is correlated to the enhanced uplift associated with the recent growth of the duplex during 8.3–1.4 Ma. GRG cooling and northward-younging of the timing of rapid cooling are observed in the results of the Duplex 02 and 03 models (Figure 12b center and right). The rapid cooling starts at 4.5 Ma and occurs at 50–200°C in the Duplex 02 model, while it starts at 7.6 Ma and occurs at 50–350°C in the Duplex 03 model. Northward-younging of the timing of the rapid cooling is apparent in each model. The rapid cooling stage corresponds to the timing of thrusting along the MHT after the duplex growth.

4.2.3. The Splay Fault Model to Test the Out-of-Sequence Thrust Model

Figures 13b and 13c illustrate the results of three Splay Fault models with varying v_{sf} of 0.0, 6.0 and 12.0 mm/yr. The *t-T* paths and FT ages from the hanging wall of the splay fault of the MHT significantly differ between the three models.

In the case of $v_{sf} = 0.0$, which corresponds to the absence of the splay fault activity, the predicted distribution patterns of the AFT and ZFT ages resemble the observed FT age distributions in eastern Nepal (Figure 13c): both the AFT and ZFT ages get older toward the north at the frontal part, then monotonously get younger toward the north at the middle and root parts. The youngest AFT and ZFT ages are predicted to occur farther north compared to the Flat-Ramp-Flat model reflecting the change in the N-S position of the mid-crustal ramp.

In the case of $v_{sf} = 6.0$ and 12.0, predicted AFT and ZFT ages are significantly younger around the surface trace of the splay fault of the MHT and become nearly constant in the hanging wall of the splay fault. This behavior of the FT ages results from the enhanced uplift of the hanging wall accompanied by the Quaternary slip of the splay fault. However, a significant gap in the ZFT ages around the splay fault appears only in the case of $v_{sf} = 12.0$, and the gap is obscure in the case of $v_{sf} = 6.0$. Such an age gap is absent in the predicted AFT ages.

The thermal effect of the enhanced uplift of the hanging wall of the splay fault of the MHT also appears in the predicted *t-T* paths. In the model without the activity of the splay fault of the MHT ($v_{sf} = 0.0$), samples from the hanging wall of the splay fault (paths 7 and 8) show GRG cooling patterns with rapid cooling phases at ca. 6 and ca. 4 Ma, respectively (Figure 13b left). In the case of enhanced uplift ($v_{sf} = 12.0$), the hanging wall does not experience GRG cooling and instead yields significant rapid cooling at ca. 2 Ma (Figure 13b right).

5. Discussion

5.1. Evaluation of the Tectono-Thermal Models Based on the Observed *t-T* Paths and FT Ages

The thermokinematic forward modeling performed in this study (Figures 8–13) reveals that a relatively simple tectono-thermal process (e.g., Coutand et al., 2014) could explain the *t-T* paths and FT age distribution patterns observed in eastern Nepal. The Flat-Ramp-Flat MHT model (Figure 9a) well reproduced the observed *t-T* paths and FT age distribution patterns (Figure 9b). In this model, the samples sequentially pass above the mid-crustal ramp as the hanging wall moves southwards, reproducing both GRG cooling and northward-younging of the timing of the rapid cooling of the observed samples (Figure 10). For the sample just above the MHT, the steep uplift above the frontal ramp causes rapid cooling in the frontmost part of the HHC nappe at the final stage. In comparison, predicted FT age distribution and *t-T* paths of the Flat MHT model are inconsistent with those observed (Figures 8b and 8c). The results of these models also indicate that the cooling process of the hanging wall of the MHT is not primarily controlled by the temporary change of v_o (Figures 8b and 8c) and the initial basal temperature (Figures 9b and 9c). Comparing the results of the Flat MHT model and the Flat-Ramp-Flat

MHT model, we consider that GRG cooling and northward-younging of the timing of the rapid cooling strongly reflect the geometry of the MHT.

In the case that the duplex structure grows as the thrust activity propagates toward the south, and that the geometry of the MHT is unstable, the *t-T* paths show neither GRG cooling nor a northward-younging trend, regardless of the presence of the flat-ramp-flat geometry in the present MHT (the Duplex 01 model; Figure 12a left). When the duplex growth imposes the first-order control on the crustal denudation processes, the samples above the duplex yield rapid cooling and do not yield a GRG cooling pattern (the Duplex 01 model; Figure 12a left). During forward propagation of the mid-crustal ramp and development of the Lesser Himalayan Duplex, GRG cooling and northward-younging trends are disturbed by the forward propagation of regions with fast exhumation rates, and this also causes younger cooling ages to appear in more foreland part of the Lesser Himalaya (this also has been shown in forward models by McQuarrie & Ehlers [2015]). For the Duplex 02 and 03 models (Figure 12a center and right), the mid-crustal ramp is located north compared to the Duplex 01 model, and the duplex and antiform grow earlier. In these cases, the *t-T* paths exhibit both GRG cooling and northward-younging resulting from long-term denudation associated with the movement of a single, stable thrust after the termination of the duplex growth. Consequently, these results indicate that the cooling process varies depending on the subsurface geometry of the decollement fault and on the timing of development of the duplex structures. In other words, regardless of the presence of a duplex or regional-scale antiform, the cooling process resembles that of the Flat-Ramp-Flat MHT model so long as the movement of a single-stable thrust postdating the duplex growth primarily controls the denudation. We interpret that the observed cooling patterns reflect the flat-ramp-flat geometry of the MHT as well as the stable geometry of the MHT in a geologic time-scale (10^6–10^7 yr).

For the Splay Fault model (Figure 13a), the Quaternary activity of the splay fault of the MHT may also disturb the GRG cooling pattern (Figure 13b). Because the uncertainties accompanying the FT ages and *t-T* paths may mask small differences, it is not easy to detect the Quaternary activity of the splay fault from the *t-T* paths if v_{sf} <6.0. However, samples from the hanging wall of the splay fault (samples EN07 and EN08) do not yield significant rapid cooling at ca. 2 Ma (paths 7 and 8 in Figure 7). The splay fault has not been recognized in eastern Nepal, therefore, we consider that the Quaternary activity of the splay fault of the MHT is not supported in this study area.

Although we did not simulate the Lateral Cooling model, we can comment on some aspects of what would be expected for the model based on the observed *t-T* paths of this study. In the case of the Lateral-Cooling model that considers the lateral-cooling of the HHC nappe enabled by the heat supply along the MCT (Figure 4d: Nakajima et al., 2020b; Sakai, 2015), the significant difference in *t-T* paths is expected depending on the structural distance from the MCT. However, there is little difference in the *t-T* path between sample EN06 from the immediate hangingwall of the MCT and sample EN07 located structurally 4 km above the MCT. Moreover, the samples located in the immediate hanging wall of the MCT (samples EN05 and EN06) yielded a GRG cooling path (paths 5 and 6) without any evidence of the heat supply. This suggests that the Lateral-Cooling model cannot account for the observation made in this study.

Consequently, we interpret that GRG cooling and northward-younging of the timing of the rapid cooling are most compatible with the tectonically-driven denudation processes reflecting: (a) denudation of the HHC nappe and underlying LHS occurred through the activity of the single thrust, (b) the thrust shows the flat-ramp-flat geometry, and (c) the geometry of the thrust was stable over a geologic time-scale (10^6–10^7 yr). As can be seen in Figure 7, GRG cooling and northward-younging pattern of the *t-T* paths are recognized as early as ca. 9 Ma. Thus, we propose that the flat-ramp-flat geometry of the current MHT was formed by ca. 9 Ma and has been more or less stable since then.

Based on the results and discussion presented above, the Flat-Ramp-Flat MHT model based on the Overthrusting model (Coutand et al., 2014; Robert et al., 2009, 2011) seems to be the most acceptable model to describe the denudation history of eastern Nepal since ca. 9 Ma. However, there remains a discrepancy between the observed *t-T* paths and the predicted *t-T* paths based on the Flat-Ramp-Flat MHT model. For example, the rapid cooling of path 8 at higher-temperature range (Figures 6a-8) is not reproduced by the forward modeling (Figure 9b). This indicates that sample EN08 remained hotter longer than predicted by the Flat-Ramp-Flat MHT model with an aid of fluid flow along the MCT, for example, as a possible heat source. It is also possible, as shown by the Splay Fault model, that rapid denudation accompanied by the local fault activity may result

in rapid cooling of sample EN08 from a hotter region (Figure 13b center and right). In addition, spatial variations in erosion potentially affect the cooling history (Olen et al., 2015). Although such a local hydrothermal, tectonothermal, and erosional process might have played a subordinate role, we consider that the denudation and cooling process of the HHC nappe was primarily controlled by the activity of the single, stable thrust with the flat-ramp-flat geometry.

5.2. Denudation History of Eastern Nepalese Himalaya

5.2.1. Duplex and Antiform Developments Before ca. 9 Ma

Since our results suggest that the geometry of the MHT has been stable since ca. 9 Ma, the development of the Tamor antiform and the Lesser Himalayan Duplex likely occurred between the termination of the MCT activity (ca. 12 Ma; Ambrose et al., 2015; Larson et al., 2017) and the initiation of the current MHT activity. Although we do not have data that directly constrain the timing of duplex development, some previous studies have inferred the timing of duplex growth: Larson et al. (2017) reported muscovite $^{40}Ar/^{39}Ar$ age of ca. 12–8 Ma from the northern margin of the Tamor window and interpreted these ages as an indicator of the development of the duplex at that period. In the Okhaldhunga window located west of the study area (Figure 1a), Nakajima et al. (2020b) pointed out that the ZFT ages exhibit a monotonous, northward-younging distribution regardless of the presence of a regional-scale antiform (Figure 3), and proposed that the timing of the antiform development was ca. 12–10 Ma. In western Bhutan, which is ∼200 km to the east of eastern Nepal, the AFT ages show northward-younging distribution, and the development of the duplex located beneath the Paro window (Figure 1a) dates back to the late Miocene (McQuarrie et al., 2014).

Considering the statements of these previous studies, the development sequence of the Lesser Himalayan Duplex in eastern Nepal can be inferred as follows: The Lesser Himalayan Duplex was built at ca. 12–10 Ma, and then was passively lifted up and over the current mid-crustal ramp. The duplex was horizontally carried above the flat by the movement along the MHT and reached at the present position. As shown by the Duplex 01 model and discussed in the previous section, the enhanced denudation of the surface was associated with the development of the duplex and antiform structures just beneath them (McQuarrie & Ehlers, 2015). The consistency between the predicted *t-T* paths with the observed ones implies that the enhanced denudation occurred at the north of the current mid-crustal ramp before ca. 9 Ma (Figure 14a, broken brown line with ?? mark).

5.2.2. Post-9 Ma Denudation Associated With the Current MHT Activity

Figure 14a shows the exhumation rate in eastern Nepal after ca. 9 Ma calculated based on the Flat-Ramp-Flat MHT model. It should be noted that topographic evolution is not taken into account and that the exhumation rate is assumed to be equal to the bedrock uplift rate in this calculation. Reflecting the geometry of the MHT, the exhumation rate exhibits a bimodal variation with a high rate (>5 mm/yr) above the frontal ramp and a middle rate (2 mm/yr) above the mid-crustal ramp. The N-S average exhumation rate of surface mesh along the section is 1.1 ± 0.9 mm/yr.

The middle exhumation rate is predicted above the mid-crustal ramp located 75–105 km north of the surface trace of the MBT (Figures 14b and 14c). This position corresponds to the highest hill slope, local relief, and specific stream power in the Arun window (Figure 1a; Olen et al., 2015) and to the highest mean annual rainfall in eastern Nepal (Bookhagen & Burbank, 2006). The peak exhumation rate of 2.1 mm/yr is comparable with the millennial-scale exhumation rate calculated from the ^{10}Be dating (up to ∼1.5 mm/yr: Olen et al., 2015). The modeled exhumation rate (Figure 14a) is also consistent with the exhumation rate in the high-mountain range estimated using thermokinematic modeling methods in central Nepal (2.3 ± 0.3 mm/yr: Robert et al., 2009; ∼2.8 mm/yr: Whipp et al., 2007), and the orogen-wide exhumation rate (1–3 mm/yr) since ca. 13 Ma constrained by the detrital thermochronology in the Bengal Fan (Figure 1b: Huyghe et al., 2020).

Since the geometry of the MHT probably did not change since ca. 9 Ma, as discussed previously, the exhumation rates in the Lesser Himalaya (0.5 mm/yr) and in the high-mountain range (2.1 mm/yr) were likely constant for about 9 Myr. The nearly constant exhumation rate of the Himalayas since the Miocene has been advocated by detrital thermochronology and ^{10}Be dating studies on a regional scale (Bernet et al., 2006; van der Beek et al., 2006) and in an orogen-wide-scale (Huyghe et al., 2020; Lenard et al., 2020). Exhumation rate changes due to factors such as changes in erosion patterns associated with climate change, and therefore, is generally not

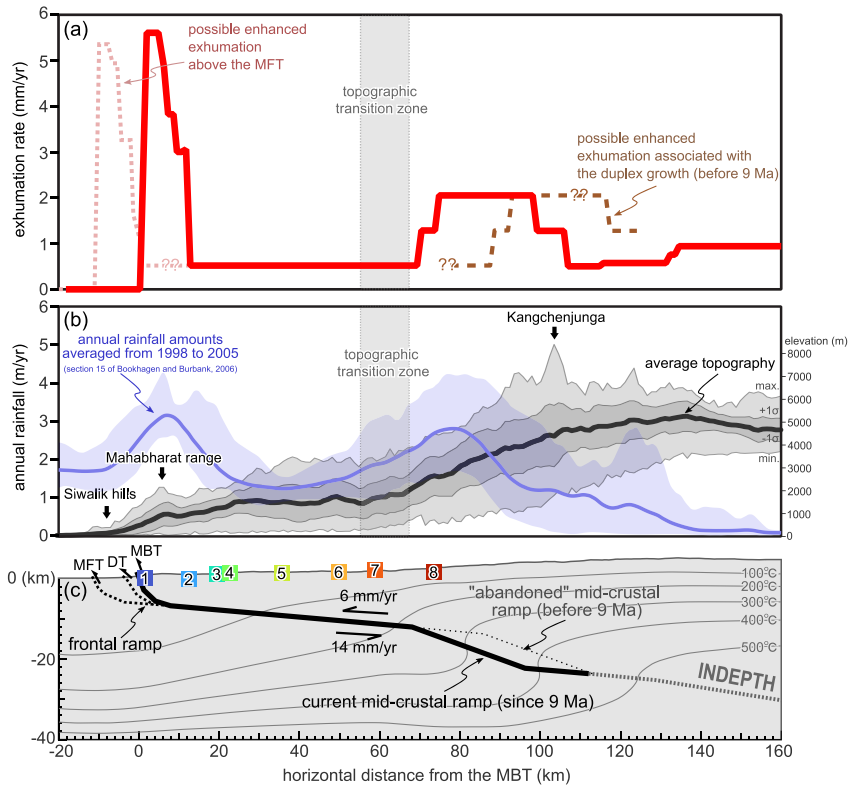

Figure 14. (a) Modeled exhumation rate distribution along the across-strike section in eastern Nepal. (b) A figure showing the mean topographic profile ± 1σ (represented by a bold black line and gray fields) and minimum/maximum elevations (represented by gray lines). Mean annual rainfall distribution ± 2σ (Section 15 of Bookhagen and Burbank [2006]) are represented by the blue bold line and blue field. (c) Cross-section of the Flat-Ramp-Flat Main Himalayan Thrust model showing model settings including the thermal field. The horizontal axes of the diagrams correspond to the horizontal distance from the Main Boundary Thrust. Numbers 1–8 represent the sample localities for *t*-*T* inversion.

considered to be constant. However, our result does not support the Quaternary enhanced denudation associated with the development of the Lesser Himalayan Duplex (Ghoshal et al., 2020; Hubbard et al., 2016) and slip of the splay fault of the MHT (Arita & Ganzawa, 1997; Blythe et al., 2007; Huntington et al., 2006) in eastern Nepal.

The sharp peaks of the exhumation rate at the Mahabharat range and the Siwalik hills (Figure 14a) reflect rapid exhumation above the frontal ramp of the MHT. The Quaternary rapid cooling of the frontmost part of the HHC nappe (sample EN01, path 1) results from the rapid exhumation above the frontal ramp. Quaternary uplift of the frontal range accompanied by the sequential thrust activity in the sub-Himalaya has been indicated by the sedimentological study of the basin-fill sediments (Sakai et al., 2006) and active fault analysis (Nakata, 1989). Young AFT ages are also reported from the frontal range of the Bhutanese Himalaya and are also considered to have resulted from the rapid exhumation above the frontal ramp of the MHT (Coutand et al., 2014).

The Quaternary thrust sequences in the sub-Himalaya are considered to vary greatly from region to region. Lavé & Avouac (2000) estimated the exhumation rate of ∼10 mm/yr in the hanging wall of the MFT (Figure 2b) in the Bagmati area, central Nepal (Figure 1a). In eastern Nepal, however, the current shortening of the crust is thought to be partly accommodated by the reactivation of the MBT rather than the MFT (Kumahara & Nakata, 2002). Therefore, the location of the current highest exhumation rate exists in the immediate hanging wall of the MBT (Figure 14a). The MBT and the MFT are considered to move in a complementary manner (Kumahara & Nakata, 2002; Thiede et al., 2017), and thus the denudation history in the Mahabharat range and the Siwalik hills is expected to be complicated.

5.3. The Linkage Between the FT Age Distribution Pattern and the Change of the MHT Geometry

An east-west, along-strike variation in terms of the geological structure, topography (Bookhagen & Burbank, 2006), and geometry of the MHT (Berger et al., 2004; Hubbard et al., 2016; Robert et al., 2011) exists in the Central and Eastern Himalayas (Figure 1a). A little along-strike variation of the FT age patterns exists as well (Figure 3). Robert et al. (2011) pointed out that the along-strike variation of the FT age patterns may reflect that in the geometry of the MHT. Our results indicate that regional differences in the timing of MHT geometry changes also contribute to regional differences in the FT age patterns. The AFT and ZFT ages exhibit the overall northward-younging in the Lesser Himalaya regardless of the position of antiform and tectonic windows in western-central Nepal, central Nepal, eastern-central Nepal, and western Bhutan (Coutand et al., 2014; Nakajima et al., 2020a, 2020b; Robert et al., 2009, 2011). In these regions, the mid-crustal ramp of the MHT is probably located beneath the high-mountain front, and the development of a duplex and antiform terminated in the Miocene (McQuarrie et al., 2014; Nakajima et al., 2020b) as observed in the study area. In contrast, in western Nepal, a young AFT age was obtained from the topographic transition zones recognized in both the northern and the southern flanks of the Karnali klippe (Figures 1a and 3; DeCelles et al., 2020; van der Beek et al., 2016). This characteristic distribution of the AFT age pattern may reflect the recent migration of the mid-crustal ramp of the MHT from north to south (Harvey et al., 2015). In the Sikkim Himalaya, the AFT ages show a nearly constant young value in the Tista half-window (Figures 1b and 3: Landry et al., 2016). Such an AFT age pattern resembles the predicted AFT age pattern of the Duplex 01 model, indicating the recent duplex growth. Reconstruction of *t-T* paths and thermokinematic modeling in this study indicate that a little along-strike variation of the FT age patterns reflects the regional variation in the geometry of the MHT, timing of mid-crustal ramp migration, and associated duplex development. Future application of reconstruction of the *t-T* paths by thermochronological inverse analysis to these regions will help constrain the 3D changes in the MHT geometry and the exhumation rate over geologic time (10^6–10^7 yr), which will help establish a more general tectono-thermal model of the Himalaya.

6. Conclusions

The AFT/ZFT datings and FT length measurements combined with thermochronological inverse analyses revealed that the cooling process of the HHC nappe distributed in eastern Nepal is characterized by the following three aspects: (a) presence of gradual-rapid-gradual (GRG) cooling, (b) northward-younging of the timing of the rapid cooling, and (c) gradual cooling followed by Quaternary rapid cooling in the frontmost part. The thermokinematic modeling elucidated that these cooling processes reflect the tectonically-driven denudation process of the hanging wall of the MHT which shows the flat-ramp-flat geometry and has been stable over millions of years. GRG cooling and northward-younging of the timing of the rapid cooling are seen after ca. 9 Ma, indicating that the flat-ramp-flat geometry of the MHT has established at ca. 9 Ma and the regional scale duplex and antiform development predated it. We consider that the exhumation rate and its spatial distribution have been stable in eastern Nepal since ca. 9 Ma.

Data Availability Statement

The newly obtained ZFT and AFT data presented in this study are available in a repository (http://dx.doi.org/10.17632/79j56f43b8.1) and Supplementary material C in Supporting Information S1 (Tables S-C1–S-C29). The GIF animation of Figure 10 also available in Movie S1.

Acknowledgments
We thank David Whipp and Kyle Larson for their constructive comments, which greatly improved the manuscript. The study was enabled by Grant-in-Aid for Scientific Research (B; No. 16H0462) and Fostering Joint International Research (B; No. 18KK0096) from the Japan Society of Promotion of Science. We would like to thank Prof. Takafumi Hirata for allowing us to use the LA–ICP–MS. We would thank Prof. Barry P. Kohn (University of Melbourne) for performing ^{252}Cf-irradiations for apatite FT dating. We also thank Mr. Lalit Rai, Mr. Harka Bahadur Majhi, and Mr. Pemba Lama Sherpa for their support in the fieldwork.

References

Ader, T., Avouac, J. P., Liu-Zeng, J., Lyon-Caen, H., Bollinger, L., Galetzka, J., et al. (2012). Convergence rate across the Nepal Himalaya and interseismic coupling on the Main Himalayan Thrust: Implications for seismic hazard. *Journal of Geophysical Research*, *117*(4). https://doi.org/10.1029/2011JB009071

Ambrose, T. K., Larson, K. P., Guilmette, C., Cottle, J. M., Buckingham, H., & Rai, S. (2015). Lateral extrusion, underplating, and out-of-sequence thrusting within the Himalayan metamorphic core, Kanchenjunga, Nepal. *Lithosphere*, *7*(4), 441–464. https://doi.org/10.1130/L437.1

Appel, E., Rösler, W., & Corvinus, G. (1991). Magnetostratigraphy of the miocene-Pleistocene Surai Khola Siwaliks in west Nepal. *Geophysical Journal International*, *105*, 191–198. https://doi.org/10.1111/j.1365-246X.1991.tb03455.x

Arita, K., & Ganzawa, Y. (1997). Thrust tectonics and uplift process of the Nepal Himalaya revealed from fission-track ages. *The Journal of Geology*, *106*(2), 156–167. https://doi.org/10.5026/jgeography.106.156

Avouac, J. P., Meng, L., Wei, S., Wang, T., & Ampuero, J. P. (2015). Lower edge of locked Main Himalayan Thrust unzipped by the 2015 Gorkha earthquake. *Nature Geoscience*, *8*(9), 708–711. https://doi.org/10.1038/ngeo2518

Berger, A., Jouanne, F., Hassani, R., & Mugnier, J. L. (2004). Modelling the spatial distribution of present-day deformation in Nepal: How cylindrical is the Main Himalayan Thrust in Nepal? *Geophysical Journal International*, *156*(1), 94–114. https://doi.org/10.1111/j.1365-246X.2004.02038.x

Bernet, M., vander Beek, P., Pik, R., Huyghe, P., Mugnier, J. L., Labrin, E., & Szulc, A. (2006). Miocene to recent exhumation of the central Himalaya determined from combined detrital zircon fission-track and U/Pb analysis of Siwalik sediments, western Nepal. *Basin Research*, *18*(4), 393–412. https://doi.org/10.1111/j.1365-2117.2006.00303.x

Bettinelli, P., Avouac, J. P., Flouzat, M., Jouanne, F., Bollinger, L., Willis, P., & Chitrakar, G. R. (2006). Plate motion of India and interseismic strain in the Nepal Himalaya from GPS and DORIS measurements. *Journal of Geodesy*, *80*(8–11), 567–589. https://doi.org/10.1007/s00190-006-0030-3

Bhattacharyya, K., & Mitra, G. (2009). A new kinematic evolutionary model for the growth of a duplex - An example from the Rangit duplex, Sikkim Himalaya, India. *Gondwana Research*, *16*(3–4), 697–715. https://doi.org/10.1016/j.gr.2009.07.006

Bilham, R., Larson, K., Freymueller, J., Jouanne, F., Le Fort, P., Leturmy, P., et al. (1997). GPS measurements of present-day convergence across the Nepal Himalaya. *Nature*, *386*, 61–64. https://doi.org/10.1038/386061a0

Blythe, A. E., Burbank, D. W., Carter, A., Schmidt, K., & Putkonen, J. (2007). Plio-Quaternary exhumation history of the central Nepalese Himalaya: 1. Apatite and zircon fission track and apatite [U-Th]/He analyses. *Tectonics*, *26*(3), TC3002. https://doi.org/10.1029/2006TC001990

Bollinger, L., Avouac, J. P., Beyssac, O., Catlos, E. J., Harrison, T. M., Grove, M., et al. (2004). Thermal structure and exhumation history of the Lesser Himalaya in central Nepal. *Tectonics*, *23*(5), TC5015. https://doi.org/10.1029/2003TC001564

Bollinger, L., Henry, P., & Avouac, J. P. (2006). Mountain building in the Nepal Himalaya: Thermal and kinematic model. *Earth and Planetary Science Letters*, *244*(1–2), 58–71. https://doi.org/10.1016/j.epsl.2006.01.045

Bookhagen, B., & Burbank, D. W. (2006). Topography, relief, and TRMM-derived rainfall variations along the Himalaya. *Geophysical Research Letters*, *33*(8), 1–5. https://doi.org/10.1029/2006GL026037

Bordet, P., Colchen, M., Krummenacher, D., Le Fort, P., Mouterde, R., & Re´my, J. M. (1971). *Recherches géologiques dans l'Himalaya du Népal, région de la Thakkhola*. CNRS.

Braun, J. (2003). Pecube: A new finite-element code to solve the 3D heat transport equation including the effects of a time-varying, finite amplitude surface topography. *Computers & Geosciences*, *29*(6), 787–794. https://doi.org/10.1016/S0098-3004(03)00052-9

Braun, J., van der Beek, P., Valla, P., Robert, X., Herman, F., Glotzbach, C., et al. (2012). Quantifying rates of landscape evolution and tectonic processes by thermochronology and numerical modeling of crustal heat transport using PECUBE. *Tectonophysics*, *524*(525), 1–28. https://doi.org/10.1016/j.tecto.2011.12.035

Carrapa, B., Robert, X., DeCelles, P. G., Orme, D. A., Thomson, S. N., & Schoenbohm, L. M. (2016). Asymmetric exhumation of the Mount Everest region: Implications for the tectono-topographic evolution of the Himalaya. *Geology*, *44*(8), 611–614. https://doi.org/10.1130/G37756.1

Catlos, E. J., Dubey, C. S., Harrison, T. M., & Edwards, M. A. (2004). Late Miocene movement within the Himalayan main central thrust shear zone, Sikkim, north-east India. *Journal of Metamorphic Geology*, *22*(3), 207–226. https://doi.org/10.1111/j.1525-1314.2004.00509.x

Catlos, E. J., Harrison, T. M., Kohn, M. J., Grove, M., Ryerson, F. J., Manning, C. E., & Upreti, B. N. (2001). Geochronologic and thermobarometric constraints on the evolution of the main central thrust, central Nepal Himalaya. *Journal of Geophysical Research*, *106*(B8), 16177–16204. https://doi.org/10.1029/2000jb900375

Catlos, E. J., Harrison, T. M., Manning, C. E., Grove, M., Rai, S. M., Hubbard, M. S., & Upreti, B. N. (2002). Records of the evolution of the Himalayan orogen from in situ Th-Pb ion microprobe dating of monazite: Eastern Nepal and Western Garhwal. *Journal of Asian Earth Sciences*, *20*(5), 459–479. https://doi.org/10.1016/S1367-9120(01)00039-6

Cattin, R., & Avouac, J. P. (2000). Modeling mountain building and the seismic cycle in the Himalaya of Nepal. *Journal of Geophysical Research*, *105*(B6), 13389–13407. https://doi.org/10.1029/2000JB900032

Coutand, I., Whipp, D. M., Grujic, D., Bernet, M., Felline, M. G., Bookhagen, B., et al. (2014). Geometry and kinematics of the Main Himalayan Thrust and Neogene crustal exhumation in the Bhutanese Himalaya derived from inversion of multithermochronologic data. *Journal of Geophysical Research: Solid Earth*, *119*, 1446–1481. https://doi.org/10.1002/2013JB010891

Crouzet, C., Dunkl, I., Paudel, L., Árkai, P., Rainer, T. M., Balogh, K., & Appel, E. (2007). Temperature and age constraints on the metamorphism of the Tethyan Himalaya in Central Nepal: A multidisciplinary approach. *Journal of Asian Earth Sciences*, *30*(1), 113–130. https://doi.org/10.1016/j.jseaes.2006.07.014

Dahlstrom, C. D. A. (1969). Balanced cross sections. *Canadian Journal of Earth Sciences*, *6*(4), 743–757. https://doi.org/10.1139/e69-069

Danhara, T., Iwano, H., Kobayashi, H., & Tsuruta, T. (2007). A report on fission-track data of zircon and apatite age-standards for age calibration using diallyl phthalate (DAP) resin detectors and a minor revision of zeta values by Danhara et al. (2003). *The Journal of the Geological Society of Japan*, *113*(2), 77–81. https://doi.org/10.5575/geosoc.113.77

Danhara, T., Iwano, H., Yoshioka, T., & Tsuruta, T. (2003). Zeta calibration values for fission track dating with a diallyl phthalate detector. *The Journal of the Geological Society of Japan*, *109*(11), 665–668. https://doi.org/10.5575/geosoc.109.665

DeCelles, P. G., Carrapa, B., Ojha, T. P., Gehrels, G. E., & Collins, D. (2020). Structural and thermal evolution of the Himalayan thrust belt in midwestern Nepal. *Geological Society of America*, *547*, 1–79. https://doi.org/10.1130/2020.2547(01)

DeCelles, P. G., Robinson, D. M., Quade, J., Ojha, T. P., Garzione, C. N., Copeland, P., & Upreti, B. N. (2001). Stratigraphy, structure, and tectonic evolution of the Himalayan fold-thrust belt in western Nepal. *Tectonics*, *20*(4), 487–509. https://doi.org/10.1029/2000TC001226

Dodson, M. H. (1973). Closure temperature in cooling geochronological and petrological systems. *Contributions to Mineralogy and Petrology*, *40*(3), 259–274. https://doi.org/10.1007/BF00373790

Duputel, Z., Vergne, J., Rivera, L., Wittlinger, G., Farra, V., & Hetényi, G. (2016). The 2015 Gorkha earthquake: A large event illuminating the Main Himalayan Thrust fault. *Geophysical Research Letters*, *43*(6), 2517–2525. https://doi.org/10.1002/2016GL068083

Elliott, J. R., Jolivet, R., González, P. J., Avouac, J. P., Hollingsworth, J., & Searle, M. P. (2016). Himalayan megathrust geometry and relation to topography revealed by the Gorkha earthquake. *Nature Geoscience*, *9*, 174–183. https://doi.org/10.1038/NGEO2623

Ghoshal, S., McQuarrie, N., Robinson, D. M., Adhikari, D. P., Morgan, L. E., & Ehlers, T. A. (2020). Constraining central Himalayan (Nepal) fault geometry through integrated thermochronology and thermokinematic modeling. *Tectonics*, *39*(9), 1–33. https://doi.org/10.1029/2020tc006399

Gilmore, M. E., McQuarrie, N., Eizenhöfer, P. R., & Ehlers, T. A. (2018). Testing the effects of topography, geometry, and kinematics on modeled thermochronometer cooling ages in the eastern Bhutan Himalaya. *Solid Earth*, *9*(3), 599–627. https://doi.org/10.5194/se-9-599-2018

Gleadow, A., Harrison, M., Kohn, B. P., Lugo-Zazueta, R., & Phillips, D. (2015). The Fish Canyon Tuff: A new look at an old low-temperature thermochronology standard. *Earth and Planetary Science Letters*, *424*, 95–108. https://doi.org/10.1016/j.epsl.2015.05.003

Gleadow, A. J. W., Duddy, I. R., Green, P. F., & Hegarty, K. A. (1986). Fission track lengths in the apatite annealing zone and the interpretation of mixed ages. *Earth and Planetary Science Letters*, *78*(2–3), 245–254. https://doi.org/10.1016/0012-821X(86)90065-8

Godard, V., Bourlès, D. L., Spinabella, F., Burbank, D. W., Bookhagen, B., Fisher, G. B., et al. (2014). Dominance of tectonics over climate in Himalayan denudation. *Geology*, *42*(3), 243–246. https://doi.org/10.1130/G35342.1

Goscombe, B., Gray, D., & Hand, M. (2006). Crustal architecture of the Himalayan metamorphic front in eastern Nepal. *Gondwana Research*, *10*(3–4), 232–255. https://doi.org/10.1016/j.gr.2006.05.003

Goscombe, B., & Hand, M. (2000). Contrasting P-T paths in the Eastern Himalaya, Nepal: Inverted isograds in a paired metamorphic mountain belt. *Journal of Petrology*, *41*(12), 1673–1719. https://doi.org/10.1093/petrology/41.12.1673

Grandin, R., Doin, M. P., Bollinger, L., Pinel-Puysségur, B., Ducret, G., Jolivet, R., & Sapkota, S. N. (2012). Long-term growth of the Himalaya inferred from interseismic InSAR measurement. *Geology*, *40*(12), 1059–1062. https://doi.org/10.1130/G33154.1

Green, P. F. (1985). Comparison of zeta calibration baselines for fission-track dating of apatite, zircon and sphene. *Chemical Geology: Isotope Geoscience section*, *58*(1–2), 1–22. https://doi.org/10.1016/0168-9622(85)90023-5

Green, P. F., & Duddy, I. (2018). Apatite (U-Th-Sm)/He thermochronology on the wrong side of the tracks. *Chemical Geology*, *488*, 21–33. https://doi.org/10.1016/j.chemgeo.2018.04.028

Groppo, C., Rolfo, F., & Lombardo, B. (2009). P-T evolution across the main central thrust zone (Eastern Nepal): Hidden discontinuities revealed by petrology. *Journal of Petrology*, *50*(6), 1149–1180. https://doi.org/10.1093/petrology/egp036

Grujic, D., Coutand, I., Bookhagen, B., Bonnet, S., Blythe, A. E., & Duncan, C. (2006). Climatic forcing of erosion, landscape, and tectonics in the Bhutan Himalayas. *Geology*, *34*(10), 801–804. https://doi.org/10.1130/G22648.1

Hames, W. E., & Bowring, S. A. (1994). An empirical evaluation of the argon diffusion geometry in muscovite. *Earth and Planetary Science Letters*, *124*(1–4), 161–169. https://doi.org/10.1016/0012-821X(94)00079-4

Harrison, T. M., Grove, M., McKeegan, K. D., Coath, C. D., Lovera, O. M., & Le Fort, P. (1999). Origin and episodic emplacement of the Manaslu intrusive complex, Central Himalaya. *Journal of Petrology*, *40*(1), 3–19. https://doi.org/10.1093/petroj/40.1.3

Harvey, J. E., Burbank, D. W., & Bookhagen, B. (2015). Along-strike changes in Himalayan thrust geometry: Topographic and tectonic discontinuities in Western Nepal. *Lithosphere*, *7*(5), 511–518. https://doi.org/10.1130/L444.1

Hasebe, N., Tagami, T., & Nishimura, S. (1994). Towards zircon fission-track thermochronology: Reference framework for confined track length measurements. *Chemical Geology*, *112*(1–2), 169–178. https://doi.org/10.1016/0009-2541(94)90112-0

Hauck, M. L., Nelson, K. D., Brown, L. D., Zhao, W., & Ross, A. R. (1998). Crustal structure of the Himalayan orogen at 90 deg east longitude from Project INDEPTH deep reflection profiles. *Tectonics*, *17*(4), 481–500. https://doi.org/10.1029/98TC01314

Herman, F., Copeland, P., Avouac, J. P., Bollinger, L., Maheo, G., Le Fort, P., et al. (2010). Exhumation, crustal deformation, and thermal structure of the Nepal Himalaya derived from the inversion of thermochronological and thermobarometric data and modeling of the topography. *Journal of Geophysical Research*, *115*(6), 1–38. https://doi.org/10.1029/2008JB006126

Hodges, K. V., Wobus, C. W., Ruhl, K., Schildgen, T., & Whipple, K. X. (2004). Quaternary deformation, river steepening, and heavy precipitation at the front of the Higher Himalayan ranges. *Earth and Planetary Science Letters*, *220*(3–4), 379–389. https://doi.org/10.1016/S0012-821X(04)00063-9

Hubbard, J., Almeida, R. V., Foster, A., Sapkota, S. N., Bürgi, P., & Tapponnier, P. (2016). Structural segmentation controlled the 2015 M_W 7.8 Gorkha earthquake rupture in Nepal. *Geology*, *44*(8), 639–642. https://doi.org/10.1130/G38077.1

Huntington, K. W., Blythe, A. E., & Hodges, K. V. (2006). Climate change and late Pliocene acceleration of erosion in the Himalaya. *Earth and Planetary Science Letters*, *252*(1–2), 107–118. https://doi.org/10.1016/j.epsl.2006.09.031

Huyghe, P., Bernet, M., Galy, A., Naylor, M., Cruz, J., Gyawali, B. R., et al. (2020). Rapid exhumation since at least 13 Ma in the Himalaya recorded by detrital apatite fission-track dating of Bengal fan (IODP Expedition 354) and modern Himalayan river sediments. *Earth and Planetary Science Letters*, *534*, 116078. https://doi.org/10.1016/j.epsl.2020.116078

Imayama, T., Takeshita, T., & Arita, K. (2010). Metamorphic P-T profile and P-T path discontinuity across the far-eastern Nepal Himalaya: Investigation of channel flow models. *Journal of Metamorphic Geology*, *28*(5), 527–549. https://doi.org/10.1111/j.1525-1314.2010.00879.x

Imayama, T., Takeshita, T., Yi, K., Cho, D. L., Kitajima, K., Tsutsumi, Y., et al. (2012). Two-stage partial melting and contrasting cooling history within the Higher Himalayan Crystalline Sequence in the far-eastern Nepal Himalaya. *Lithos*, *134*(135), 1–22. https://doi.org/10.1016/j.lithos.2011.12.004

Imayama, T., Takeshita, T., Yi, K., & Fukuyama, M. (2019). Early Oligocene partial melting via biotite dehydration melting and prolonged low-pressure–low-temperature metamorphism of the upper High Himalaya Crystalline Sequence in the far east of Nepal. *Geological Society, London, Special Publications*, *481*(1), 147–173. https://doi.org/10.1144/sp481.2

Inger, S., & Harris, N. B. W. (1992). Tectonothermal evolution of the High Himalayan crystalline sequence, Langtang valley, northern Nepal. *Journal of Metamorphic Geology*, *10*(3), 439–452. https://doi.org/10.1111/j.1525-1314.1992.tb00095.x

Jackson, M., & Bilham, R. (1994). Constraints on Himalayan deformation inferred from vertical velocity fields in Nepal and Tibet. *Journal of Geophysical Research*, *99*(B7), 13897–13914. https://doi.org/10.1029/94jb00714

Jouanne, F., Mugnier, J. L., Gamond, J. F., Le Fort, P., Pandey, M. R., Bollinger, L., et al. (2004). Current shortening across the Himalayas of Nepal. *Geophysical Journal International*, *157*(1), 1–14. https://doi.org/10.1111/j.1365-246X.2004.02180.x

Kawakami, T., Sakai, H., & Sato, K. (2019). Syn-metamorphic B-bearing fluid infiltrations deduced from tourmaline in the main central thrust zone, eastern Nepal Himalayas. *Lithos*, *348*, 1–16. https://doi.org/10.1016/j.lithos.2019.105175

Ketcham, R. A. (2005). Forward and inverse modeling of low-temperature thermochronometry data. *Reviews in Mineralogy and Geochemistry*, *58*(1), 275–314. https://doi.org/10.2138/rmg.2005.58.11

Ketcham, R. A., Carter, A., Donelick, R. A., Barbarand, J., & Hurford, A. J. (2007). Improved modeling of fission-track annealing in apatite. *American Mineralogist*, *92*(5–6), 799–810. https://doi.org/10.2138/am.2007.2281

Ketcham, R. A., Carter, A., & Hurford, A. J. (2015). Inter-laboratory comparison of fission track confined length and etch figure measurements in apatite. *American Mineralogist*, *100*(7), 1452–1468. https://doi.org/10.2138/am-2015-5167

Ketcham, R. A., Malusà, M. G., & Fitzgerald, P. G. (2019). *Fission-track thermochronology and its application to geology* (pp. 49–75). Springer. https://doi.org/10.1007/978-3-319-89421-8_3

Khanal, S., & Robinson, D. M. (2013). Upper crustal shortening and forward modeling of the Himalayan thrust belt along the Budhi-Gandaki River, central Nepal. *International Journal of Earth Sciences*, *102*(7), 1871–1891. https://doi.org/10.1007/s00531-013-0889-1

Khanal, S., Robinson, D. M., Kohn, M. J., & Mandal, S. (2015). Evidence for a far-traveled thrust sheet in the Greater Himalayan thrust system, and an alternative model to building the Himalaya. *Tectonics*, *34*(1), 31–52. https://doi.org/10.1002/2014TC003616

Kobayashi, W., Sakai, H., Iwano, H., Danhara, T., & Hirata, T. (2021). Non-metamorphosed autochthonous kuncha-Naudanda-Heklang formations and their differences from those of the kuncha nappe: A multichronological approach. *Island Arc*, *30*, e12396. https://doi.org/10.1111/iar.12396

Kohn, M. J., Catlos, E. J., Ryerson, F. J., & Harrison, T. M. (2001). Pressure-temperature-time path discontinuity in the Main Central thrust zone, central Nepal. *Geology*, *29*(7), 571–574. https://doi.org/10.1130/0091-7613(2001)029<0571:pttpdi>2.0.co;2

Kumahara, Y., & Nakata, T. (2002). Distribution and faulting activity of Himalayan front active faults investigated by interpretation of spy satellite photographs. *Chikyu Monthly*, *24*, 254–258.

Landry, K. R., Coutand, I., Whipp, D. M., Grujic, D., & Hourigan, J. K. (2016). Late Neogene tectonically driven crustal exhumation of the Sikkim Himalaya: Insights from inversion of multithermochronologic data. *Tectonics*, *35*(3), 831–857. https://doi.org/10.1002/2015TC004102

Larson, K. P., Camacho, A., Cottle, J. M., Coutand, I., Buckingham, H. M., Ambrose, T. K., & Rai, S. M. (2017). Cooling, exhumation, and kinematics of the Kanchenjunga Himal, far east Nepal. *Tectonics*, *36*(6), 1037–1052. https://doi.org/10.1002/2017TC004496

Lavé, J., & Avouac, J. P. (2000). Active folding of fluvial terraces across the Siwaliks hills, Himalayas of central Nepal. *Journal of Geophysical Research*, *105*(B3), 5735–5770. https://doi.org/10.1029/1999jb900292

Lavé, J., & Avouac, J. P. (2001). Fluvial incision and tectonic uplift across the Himalayas of central Nepal. *Journal of Geophysical Research*, *106*(B11), 26561–26591. https://doi.org/10.1029/2001jb000359

Le Fort, P. (1975). Himalayas: The collided range. Present knowledge of the continental arc. *American Journal of Science*, *275*, 1–44.

Leloup, P. H., Mahéo, G., Arnaud, N., Kali, E., Boutonnet, E., Liu, D., et al. (2010). The South Tibet detachment shear zone in the Dinggye area. Time constraints on extrusion models of the Himalayas. *Earth and Planetary Science Letters*, *292*(1–2), 1–16. https://doi.org/10.1016/j.epsl.2009.12.035

Lenard, S. J. P., Lavé, J., France-Lanord, C., Aumaître, G., Bourlès, D. L., & Keddadouche, K. (2020). Steady erosion rates in the Himalayas through late Cenozoic climatic changes. *Nature Geoscience*, *13*(6), 448–452. https://doi.org/10.1038/s41561-020-0585-2

Long, S. P., McQuarrie, N., Tobgay, T., Coutand, I., Cooper, F. J., Reiners, P. W., et al. (2012). Variable shortening rates in the eastern Himalayan thrust belt, Bhutan: Insights from multiple thermochronologic and geochronologic data sets tied to kinematic reconstructions. *Tectonics*, *31*(5), 1–23. https://doi.org/10.1029/2012TC003155

Long, S. P., McQuarrie, N., Tobgay, T., & Grujic, D. (2011). Geometry and crustal shortening of the Himalayan fold-thrust belt, eastern and central Bhutan. *Bulletin of the Geological Society of America*, *123*(7–8), 1427–1447. https://doi.org/10.1130/B30203.1

Mahato, S. P. (2011). *Geological map of eastern Nepal*. Map, Geological Mapping Section, Department of Mines and Geology.

McQuarrie, N., & Ehlers, T. A. (2015). Influence of thrust belt geometry and shortening rate on thermochronometer cooling ages: Insights from thermokinematic and erosion modeling of the Bhutan Himalaya. *Tectonics*, *34*(6), 1055–1079. https://doi.org/10.1002/2014TC003783

McQuarrie, N., Eizenhöfer, P. R., Long, S. P., Tobgay, T., Ehlers, T. A., Blythe, A. E., et al. (2019). The influence of foreland structures on hinterland cooling: Evaluating the drivers of exhumation in the eastern Bhutan Himalaya. *Tectonics*, *38*(9), 3282–3310. https://doi.org/10.1029/2018tc005340

McQuarrie, N., Tobgay, T., Long, S. P., Reiners, P. W., & Cosca, M. A. (2014). Variable exhumation rates and variable displacement rates: Documenting recent slowing of Himalayan shortening in western Bhutan. *Earth and Planetary Science Letters*, *386*, 161–174. https://doi.org/10.1016/j.epsl.2013.10.045

Meigs, A. J., Burbank, D. W., & Beck, R. A. (1995). Middle–late Miocene (>10 Ma) formation of the Main Boundary thrust in the western Himalaya. *Geology*, *23*, 4232–4426. https://doi.org/10.1130/0091-7613(1995)023<0423:mlmmfo>2.3.co;2

Mendoza, M. M., Ghosh, A., Karplus, M. S., Klemperer, S. L., Sapkota, S. N., Adhikari, L. B., & Velasco, A. (2019). Duplex in the Main Himalayan Thrust illuminated by aftershocks of the 2015 Mw 7.8 Gorkha earthquake. *Nature Geoscience*, *12*(12), 1018–1022. https://doi.org/10.1038/s41561-019-0474-8

Mitra, S., Priestley, K., Bhattacharyya, A. K., & Gaur, V. K. (2005). Crustal structure and earthquake focal depths beneath northeastern India and southern Tibet. *Geophysical Journal International*, *160*(1), 227–248. https://doi.org/10.1111/j.1365-246X.2004.02470.x

Mukul, M., Jade, S., Bhattacharyya, A. K., & Bhusan, K. (2010). Crustal shortening in convergent orogens: Insights from global positioning system (GPS) measurements in Northeast India. *Journal of the Geological Society of India*, *75*(1), 302–312. https://doi.org/10.1007/s12594-010-0017-9

Mukul, M., Jaiswal, M., & Singhvi, A. K. (2007). Timing of recent out-of-sequence active deformation in the frontal Himalayan wedge: Insights from the Darjiling sub-Himalaya, India. *Geology*, *35*(11), 999–1002. https://doi.org/10.1130/G23869A.1

Nábělek, J., Hetényi, G., Vergne, J., Sapkota, S., Kafle, B., Jiang, M., et al. (2009). Underplating in the himalaya-tibet collision zone revealed by the Hi-CLIMB experiment. *Science*, *325*(5946), 1371–1374. https://doi.org/10.1126/science.1167719

Nadin, E. S., & Martin, A. J. (2012). Apatite thermochronometry within a knickzone near the Higher Himalaya front, central Nepal: No resolvable fault motion in the past one million years. *Tectonics*, *31*(2), 1–11. https://doi.org/10.1029/2011TC003000

Naito, N., Ageta, Y., Iwata, S., Matsuda, Y., Suzuki, R., & Yabuki, H. (2006). Glacier shrinkages and climate conditions around Jichu Dramo glacier in the Bhutan Himalayas from 1998 to 2003. *Bulletin of Glaciological Research*, *23*, 51–61.

Nakajima, T., Sakai, H., Iwano, H., Danhara, T., & Hirata, T. (2020a). Northward cooling of the Kuncha nappe and downward heating of the Lesser Himalayan autochthon distributed to the south of Mt. Annapurna, Western central Nepal. *Island Arc*, *29*(e12349), 1–15. https://doi.org/10.1111/iar.12349

Nakajima, T., Sakai, H., Iwano, H., Danhara, T., & Hirata, T. (2020b). Northward younging zircon fission-track ages from 13 to 2 Ma in the eastern extension of the Kathmandu nappe and underlying Lesser Himalayan sediments distributed to the south of Mt. Everest. *Island Arc*, *29*(1), e12352. https://doi.org/10.1111/iar.12352

Nakata, T. (1989). Active faults of the Himalaya of India and Nepal. In L. L. Malinconico & R. J. Lillie (Eds.), *Tectonics of the western Himalayas* (Vol. 232, p. 0). Geological Society of America. https://doi.org/10.1130/SPE232-p243

Olen, S. M., Bookhagen, B., Hoffmann, B., Sachse, D., Adhikari, D. P., & Strecker, M. R. (2015). Understanding erosion rates in the Himalayan orogen: A case study from the Arun Valley. *Journal of Geophysical Research: Earth Surface*, *120*(10), 2080–2102. https://doi.org/10.1002/2014jf003410

Parrish, R. R., & Hodges, K. V. (1996). Isotopic constraints on the age and provenance of the Lesser and Greater Himalayan sequences, Nepalese Himalaya. *Bulletin of the Geological Society of America*, *108*, 9042–9911. https://doi.org/10.1130/0016-7606(1996)108<0904:icotaa>2.3.co;2

Pearson, O. N., & DeCelles, P. G. (2005). Structural geology and regional tectonic significance of the Ramgarh thrust, Himalayan fold-thrust belt of Nepal. *Tectonics*, *24*(4), 1–26. https://doi.org/10.1029/2003TC001617

Pecher, A. (1989). The metamorphism in the central Himalaya. *Journal of Metamorphic Geology*, *7*(1), 31–41. https://doi.org/10.1111/j.1525-1314.1989.tb00573.x

Rai, L. K., Acharya, K. K., & Dhital, M. R. (2016). Lithostratigraphy and structure of the Dharan–Mulghat area, Lesser Himalayan sequence, eastern Nepal Himalaya. *Journal of Nepal Geological Society*, *51*, 77–78. https://doi.org/10.3126/jngs.v51i0.24095

Reiners, P. W., & Ehlers, T. A. (Eds.). (2005). *Low-temperature thermochronology: Techniques, interpretations, and applications*. Mineralogical Society of America.

Ring, U., Brandon, M. T., Willett, S. D., & Lister, G. S. (1999). Exhumation processes. *Geological Society Special Publication*, *154*, 1–27. https://doi.org/10.1144/GSL.SP.1999.154.01.01

Robert, X., van der Beek, P., Braun, J., Perry, C., Dubille, M., & Mugnier, J. L. (2009). Assessing quaternary reactivation of the Main Central thrust zone (central Nepal Himalaya): New thermochronologic data and numerical modeling. *Geology*, *37*(8), 731–734. https://doi.org/10.1130/G25736A.1

Robert, X., van der Beek, P., Braun, J., Perry, C., & Mugnier, J. L. (2011). Control of detachment geometry on lateral variations in exhumation rates in the Himalaya: Insights from low-temperature thermochronology and numerical modeling. *Journal of Geophysical Research*, *116*(5), 1–22. https://doi.org/10.1029/2010JB007893

Sakai, H. (1983). *Geology of the Tansen group of the Lesser Himalaya in Nepal* (Vol. 25, pp. 27–74). Memoirs of the Faculty of Science, Kyushu University. https://doi.org/10.5109/1546083

Sakai, H. (2005). Uplift of the Himalayan range and Tibetan Plateau-From a viewpoint of birth of monsoon system and its changes. *The Journal of the Geological Society of Japan*, *111*(11), 701–716. https://doi.org/10.5575/geosoc.111.701

Sakai, H. (2015). Tectonics of the collided range of the Himalaya: Recent advance and a new scenario. *Kagaku*, *85*, 956–962.

Sakai, H., Imayama, T., Yoshida, K., & Asahi, K. (2017). Tectonics of the Himalayas. *The Journal of the Geological Society of Japan*, *123*, 403–421. https://doi.org/10.5575/geosoc.2017.0026

Sakai, H., Iwano, H., Danhara, T., Hirata, T., & Takigami, Y. (2013). Emplacement of hot Lesser Himalayan nappes from 15 to 10 Ma in the Jumla-Surkhet region, Western Nepal, and their thermal imprint on the underlying Early Miocene Fluvial Dumri Formation. *Island Arc*, *22*(3), 361–381. https://doi.org/10.1111/iar.12030

Sakai, H., Iwano, H., Danhara, T., Takigami, Y., Rai, S. M., Upreti, B. N., & Hirata, T. (2013). Rift-related origin of the Paleoproterozoic Kuncha Formation, and cooling history of the Kuncha nappe and Taplejung granites, eastern Nepal Lesser Himalaya: A multichronological approach. *Island Arc*, *22*(3), 338–360. https://doi.org/10.1111/iar.12021

Sakai, H., Sakai, H., Yahagi, W., Fujii, R., Hayashi, T., & Upreti, B. N. (2006). Pleistocene rapid uplift of the Himalayan frontal ranges recorded in the Kathmandu and Siwalik basins. *Palaeogeography, Palaeoclimatology, Palaeoecology*, *241*(1), 16–27. https://doi.org/10.1016/j.palaeo.2006.06.017

Sakai, H., Sawada, M., Takigami, Y., Orihashi, Y., Danhara, T., Iwano, H., et al. (2005). Geology of the summit limestone of Mount Qomolangma (Everest) and cooling history of the Yellow Band under the Qomolangma detachment. *Island Arc*, *14*(4), 297–310. https://doi.org/10.1111/j.1440-1738.2005.00499.x

Sato, K., Sakai, H., & Kawakami, T. (2019). Distribution of ductile deformation around the Main Central Thrust zone at the frontal part of nappe in southeastern Nepal Himalaya. *Island Arc*, *29*(1), e12333. https://doi.org/10.1111/iar.12333

Schelling, D. (1992). The tectonostratigraphy and structure of the Eastern Nepal Himalaya. *Tectonics*, *11*(5), 925–943. https://doi.org/10.1029/92TC00213

Schelling, D., & Arita, K. (1991). Thrust tectonics, crustal shortening, and the structure of the far-eastern Nepal Himalaya. *Tectonics*, *10*(5), 851–862. https://doi.org/10.1029/91TC01011

Schulte-Pelkum, V., Monsalve, G., Sheehan, A., Pandey, M. R., Sapkota, S., Bilham, R., & Wu, F. (2005). Imaging the Indian subcontinent beneath the Himalaya. *Nature*, *435*(7046), 1222–1225. https://doi.org/10.1038/nature03678

Schultz, M. H., Hodges, K. V., Ehlers, T. A., Van Soest, M. C., & Wartho, J. A. (2017). Thermochronologic constraints on the slip history of the South Tibetan detachment system in the Everest region, southern Tibet. *Earth and Planetary Science Letters*, *459*, 105–117. https://doi.org/10.1016/j.epsl.2016.11.022

Shrestha, S. B., Shrestha, J. N., & Sharma, S. R. (1984). *Geological map of eastern Nepal* (Vol. 1, p. 250). Ministry of Industry, Department of Mines and Geology.

Soucy La Roche, R., Godin, L., Cottle, J. M., & Kellett, D. A. (2018). Preservation of the early evolution of the Himalayan middle crust in foreland klippen: Insights from the Karnali klippe, west Nepal. *Tectonics*, *37*(5), 1161–1193. https://doi.org/10.1002/2017TC004847

Streule, M. J., Carter, A., Searle, M. P., & Cottle, J. M. (2012). Constraints on brittle field exhumation of the Everest-Makalu section of the Greater Himalayan Sequence: Implications for models of crustal flow. *Tectonics*, *31*(3), 1–14. https://doi.org/10.1029/2011TC003062

Thiede, R. C., & Ehlers, T. A. (2013). Large spatial and temporal variations in Himalayan denudation. *Earth and Planetary Science Letters*, *371–372*, 278–293. https://doi.org/10.1016/j.epsl.2013.03.004

Thiede, R. C., Robert, X., Stübner, K., Dey, S., & Faruhn, J. (2017). Sustained out-of-sequence shortening along a tectonically active segment of the Main Boundary thrust: The Dhauladhar Range in the northwestern Himalaya. *Lithosphere*, *9*(5), 715–725. https://doi.org/10.1130/L630E.1

van der Beek, P., Litty, C., Baudin, M., Mercier, J., Robert, X., & Hardwick, E. (2016). Contrasting tectonically driven exhumation and incision patterns, Western versus central Nepal Himalaya. *Geology*, *44*(4), 327–330. https://doi.org/10.1130/G37579.1

van der Beek, P., Robert, X., Mugnier, J. L., Bernet, M., Huyghe, P., & Labrin, E. (2006). Late Miocene–Recent exhumation of the central Himalaya and recycling in the foreland basin assessed by apatite fission-track thermochronology of Siwalik sediments, Nepal. *Basin Research*, *18*(4), 413–434. https://doi.org/10.1111/j.1365-2117.2006.00305.x

Wang, A., Garver, J. I., Wang, G., Smith, J. A., & Zhang, K. (2010). Episodic exhumation of the Greater Himalayan Sequence since the Miocene constrained by fission track thermochronology in Nyalam, central Himalaya. *Tectonophysics*, *495*(3–4), 315–323. https://doi.org/10.1016/j.tecto.2010.09.037

Wang, X., Wei, S., & Wu, W. (2017). Double-ramp on the Main Himalayan Thrust revealed by broadband waveform modeling of the 2015 Gorkha earthquake sequence. *Earth and Planetary Science Letters*, *473*, 83–93. https://doi.org/10.1016/j.epsl.2017.05.032

Whipp, D. M., Ehlers, T. A., Blythe, A. E., Huntington, K. W., Hodges, K. V., & Burbank, D. W. (2007). Plio-Quaternary exhumation history of the central Nepalese himalaya: 2. Thermokinematic and thermochronometer age prediction model. *Tectonics*, *26*(3), 1–23. https://doi.org/10.1029/2006TC001991

Whipp, D. M., Kellett, D. A., Coutand, I., & Ketcham, R. A. (2022). Modeling competing effects of cooling rate, grain size, and radiation damage in low-temperature thermochronometers. *Geochronology*, *4*(1), 143–152. https://doi.org/10.5194/gchron-4-143-2022

Whipple, K. X., Shirzaei, M., Hodges, K. V., & Ramon Arrowsmith, J. (2016). Active shortening within the Himalayan orogenic wedge implied by the 2015 Gorkha earthquake. *Nature Geoscience*, *9*(9), 711–716. https://doi.org/10.1038/ngeo2797

Wobus, C. W., Hodges, K. V., & Whipple, K. X. (2003). Has focused denudation sustained active thrusting at the Himalayan topographic front? *Geology*, *31*(10), 861–864. https://doi.org/10.1130/G19730.1

Wobus, C. W., Whipple, K. X., & Hodges, K. V. (2006). Neotectonics of the central Nepalese Himalaya: Constraints from geomorphology, detrital $^{40}Ar/^{39}Ar$ thermochronology, and thermal modeling. *Tectonics*, *25*(4), 1–18. https://doi.org/10.1029/2005TC001935

Yamada, R., Tagami, T., & Nishimura, S. (1995). Confined fission-track length measurement of zircon: Assessment of factors affecting the paleotemperature estimate. *Chemical Geology*, *119*, 293–306. https://doi.org/10.1016/0009-2541(94)00108-K

Yamada, R., Tagami, T., Nishimura, S., & Ito, H. (1995). Annealing kinetics of fission tracks in zircon: An experimental study. *Chemical Geology*, *122*(1–4), 249–258. https://doi.org/10.1016/0009-2541(95)00006-8

Zhao, W., Nelson, K. D., Che, J., Quo, J., Lu, D., Wu, C., & Liu, X. (1993). Deep seismic reflection evidence for continental underthrusting beneath southern Tibet. *Nature*, *366*(6455), 557–559. https://doi.org/10.1038/366557a0